X-Ray Scattering Point Models for Breast Cone-Beam Computed Tomography

by

Curtis Laamanen

A thesis submitted in partial fulfillment
of the requirements for the degree of
Master of Science (MSc) in Physics

The Faculty of Graduate Studies
Laurentian University
Sudbury, Ontario, Canada

THESIS DEFENCE COMMITTEE/COMITÉ DE SOUTENANCE DE THÈSE
Laurentian Université/Université Laurentienne
Faculty of Graduate Studies/Faculté des études supérieures

Title of Thesis Titre de la thèse	X-Ray Scattering Point Models for Breast Cone-Beam Computed Tomography
Name of Candidate Nom du candidat	Laamanen, Curtis
Degree Diplôme	Master of Science
Department/Program Département/Programme	Physics
Date of Defence Date de la soutenance	March 1, 2016

APPROVED/APPROUVÉ

Thesis Examiners/Examinateurs de thèse:

Dr. Eduardo Galiano-Riveros
(Supervisor/Directeur(trice) de thèse)

Dr. Clarence Virtue
(Committee member/Membre du comité)

Dr. Paul Johns
(External Examiner/Examinateur externe)

Approved for the Faculty of Graduate Studies
Approuvé pour la Faculté des études supérieures
Dr. David Lesbarrères
Monsieur David Lesbarrères
Dean, Faculty of Graduate Studies
Doyen, Faculté des études supérieures

ACCESSIBILITY CLAUSE AND PERMISSION TO USE

Abstract

The purpose of this work was to determine via simulations the potential use of simplified scattering point models in full-field breast Cone-Beam Computed Tomography (CBCT).

A many Scattering Point (MSP) per incident beamlet model and a Single Scattering Point (SSP) model were tested against Geant4 simulations, as well as against each other. Comparisons were made using both homogeneous as well as heterogeneous phantoms. The homogeneous phantoms were cylinders, 14 cm and 7 cm in diameter and 10.5 cm in length with various fibroglandular(fib):fat compositions. The heterogeneous phantom was the 14 cm phantom mentioned previously, but modeled as pure fib with a number of smaller embedded cylinders composed of fat. A second configuration with the compositions of the main and embedded cylinders swapped was also tested. The simulation used a 60 kV tungsten anode spectrum with a HVL of 3.7 mm Al which irradiated the simulated breast phantom over 300 projections. The detector was modeled as 300×300, 1 mm^2 energy integrating pixels, with a DQE of unity. Both of the models approximate the cone-beam as a number of individual beamlets (300×300 to match with the detector) with scattering points placed along their intersections with the phantom. The MSP model incorporated a single scattering point per 1 cm of incident beamlet length within the phantom. The SSP model used an adjustable single scattering point positioned at a fractional depth δ within the phantom. By comparing results from these two scattering point models, values of δ were determined which would yield SSP model scatter approximations matching those of

the MSP model. Both models were tested against Geant4 simulations for their ability to adequately estimate the scatter signals upon the detector. The SSP model was also tested for its ability to correct for the cupping artifact in reconstructed images of the heterogeneous phantom, without assuming knowledge of the inner heterogeneous geometry.

The Hounsfield Units (HU) obtained with primary photons were 48.5 ± 3.18 and -159 ± 23.0 for fib and fat respectively for one of the heterogeneous phantom configurations. Due to the cupping artifact in the reconstructed images which included scatter, these values were -46.6 ± 18.9 and -215 ± 34.0 respectively. Following corrections for the single scatter, via the SSP model, the corresponding CT numbers became 52.3 ± 3.67 and -161 ± 23.3.

It was encouraging to see that a simple model can minimize the effects of single scattered photons during CBCT of a heterogeneous phantom. The HUs obtained post-scatter correction agreed well with those obtained with primary photons. The preliminary findings encourage further efforts for thoroughly testing these scatter point models' applicability for obtaining higher quality CBCT images.

Acknowledgements

Above all else, I would like to thank my family for their continued support through the entirety of my education. They were always with me through the toughest times, and without them this research wouldn't have been possible.

I would also like to extend my deepest gratitude towards my supervisors Dr. Galiano and Dr. LeClair for their continued guidance throughout my time at Laurentian. The support of the faculty and fellow students at Laurentian University has been key to the completion of my masters.

Contents

Thesis Defence Committee ii

Abstract iii

Acknowledgements v

Table of Contents vi

Contents vi

List of Figures ix

List of Tables xi

List of Symbols and Abbreviations xii

1 Introduction 1

1.1 Cone-Beam Computed Tomography 2

1.2 Literature 6

1.3 Thesis Outline 7

2 Physics of X-ray Interactions in Diagnostic Imaging **9**

2.1 X-ray Attenuation 10

2.2 Photoelectric Absorption 12

2.3 Compton Scatter 14

2.4 Rayleigh Scatter 16

2.5 Pair Production 19

2.6 X-ray Properties of Breast Tissue 20

3 X-ray Models **23**

3.1 Scattering Point Models 23

3.1.1 Many Scattering Point Model 25

3.1.2 Single Scattering Point Model 27

3.2 Geant4 Monte Carlo Model 29

4 Methodology **31**

4.1 Simulation Geometry 31

4.2 Validation of Scattering Point Models 35

4.2.1 Geant4 Simulations 35

4.2.2 MSP Model 36

4.2.3 SSP Model 37

4.3 Potential Use of the SSP Model 38

5 Results **43**

5.1 Validation of Scattering Point Models 43

5.1.1 MSP versus Geant4 43

5.1.2 SSP versus Geant4 45
5.1.3 SSP versus MSP 46
5.2 Potential Use of the SSP Model 50
5.2.1 14 cm Diameter Cylinder with 21 Embedded Small Axial Cylinders 50
5.2.2 14 cm Diameter Cylinder with 5 Large Embedded Cylinders . 53

6 Discussion **60**

7 Conclusion **62**

A MSP Model Code Segment **64**

B On the Concept of KERMA and Absorbed Dose **69**

References **71**

List of Figures

1.1 Schematic of CBCT geometry. 3

1.2 Example of a cupping artifact in reconstructed images. 5

2.1 Basic x-ray attenuation diagram. 11

2.2 Photoelectric absorption diagram. 13

2.3 Compton scatter diagram. 14

2.4 Rayleigh scatter diagram. 17

2.5 Coherent scattering functions of breast tissue. 19

2.6 Pair production diagram. 20

2.7 Attenuation values of breast tissue. 21

3.1 Pencil beam scatter schematic. 24

3.2 Many Scattering Point Model schematic. 26

3.3 Single Scattering Point Model schematic. 28

4.1 Simulated phantoms. 32

4.2 Simulated spectrum. 34

5.1 Central slice SPRs as simulated by Geant4. 44

5.2 EIS_s ratios showing effects of Compton shift and diffraction effects. . 44

5.3 Using Geant4 results to find δ values for the SSP model. 46

5.4 Comparison between Geant4 and SSP model results. 47

5.5 SPR results via the MSP model for various phantom compositions. . 48

5.6 Results of δ vs ν_{fib} for simulated phantoms. 49

5.7 Comparison between MSP and SSP results across phantom length. . . 51

5.8 Reconstructed images & image profiles, phantom design B. 52

5.9 HU values of reconstructed axial cylinders. 54

5.10 SSP vs MSP ratios, including effects of choosing an incorrect SSP δ. . 55

5.11 Reconstructed images, phantom design A. 56

5.12 Line profiles of images shown in Fig. 5.11. 57

List of Tables

4.1 Specifications of embedded cylinders of phantom B. 32

5.1 Table of HU values showing effects of scatter & scatter correction. . . 59

List of Symbols and Abbreviations

Abbreviations

CBCT	Cone-Beam Computed Tomography
EIS	Energy Integrated Signal
SPR	Scatter to Primary Ratio
HVL	Half Value Layer
HU	Hounsfield Units
fib	Fibroglandular tissue
fat	Fatty (or adipose) tissue
MSP	Many Scattering Point (model)
SSP	Single Scattering Point (model)
IAM	Independent Atomic Model (data)
Diff	Diffraction (data)

Symbols

m	Mass fraction
ν	Volume fraction
E	Photon energy
θ	Scattering angle
$N(E)$	Number of photons of energy E
$N_p(E)$	Number of primary photons (have not undergone an interaction event)
$N_s(E)$	Number of scattered photons
$N_t(E)$	Combined number of primary and scattered photons
$\mu(E)$	Attenuation coefficient
$\frac{\mathrm{d}\sigma}{\mathrm{d}\Omega}(E,\theta)$	Differential angular cross section
$\frac{\mathrm{d}\mu_s}{\mathrm{d}\Omega}(E,\theta)$	Differential linear scattering coefficient
$F_{\mathrm{KN}}(E,\theta)$	Klein-Nishina formula
$S(x)$	Incoherent atomic form factor
$F(x)$	Coherent atomic form factor
x	Momentum transfer variable
r_0	Classical electron radius
ρ_e	Electron density
σ	Cross section
Ω	Solid angle
λ	Radon transform
δ	Adjustment parameter in the SSP model

Chapter 1

Introduction

The Canadian Cancer Society estimates that in 2015 there will be 78000 deaths due to cancer in Canada, along with 196900 new cases of cancer diagnosed.[1] These deaths due to cancer make up 30% of the mortality rate in Canada. For women in Canada specifically, it is expected that over the course of their lives 42% of women in Canada will develop cancer, and 24% of women will die from it. Breast cancer accounts for about one quarter (26%) of all new cancer cases in women. In order to both diagnose and treat all types of cancer cases, medical imaging is of vital importance.

X-ray imaging is the most common form of cancer imaging for both diagnostic and treatment purposes. For breast cancer, the most common imaging method in the past has been breast mammography, which obtains a single transmission image of a compressed breast. However, this imaging method has a major drawback from the superposition of overlapping breast structures in the resultant images, which can make interpretation difficult. The development of Computed Tomography (CT) imaging techniques has overcome this shortcoming by allowing reconstruction of arbitrary image slices through 3D space, or with further processing, reconstruction of a virtual 3D object. These resulting visualizations remove the issue of structural superposition. They tend however to require more complex instrumentation and longer acquisition

times.

1.1 Cone-Beam Computed Tomography

A major focal point of research into CT imaging is the development of Cone-Beam Computed Tomography (CBCT). The cone-beam CT imaging technique allows acquisition of CT images while incurring a mean glandular dose comparable to mammography [2], and still remaining reasonably competitive for imaging times. The general concept of CBCT imaging is that a large number of projection images (often up to 300) are taken at various rotational steps about the breast using a wide-angle cone shaped beam. Using these projections, the desired image slices may be reconstructed. Generally speaking, the process of obtaining cone-beam CT images can be described as consisting of three main steps: the projection-image acquisition, the filtering of these projections, and finally the reconstruction of the image.

The first step in CBCT imaging, and the only physical step, is the acquisition of the projection images. A simple schematic of the general geometry of a CBCT imaging system is shown in Fig. 1.1. Projection images are acquired as the transmitted x-ray signal upon the detector. Most commonly, these projection images are taken via a step-and-shoot method where the x-ray source and detector are rotated by a set amount before stopping, and remaining still to capture the projection image. [3] An alternative acquisition method being developed is continuous acquisition where the projection images are acquired while the imaging apparatus continues rotation. This second method allows for faster acquisition times since there is no 'wasted' time compared to the step-and-shoot method; however it does come at the cost of reduced rotational resolution, which needs to be accounted for later during the reconstruction. In this thesis, the step-and-shoot method is used for all scenarios. The acquisition method is not of great significance to this work, however the step-and-shoot method

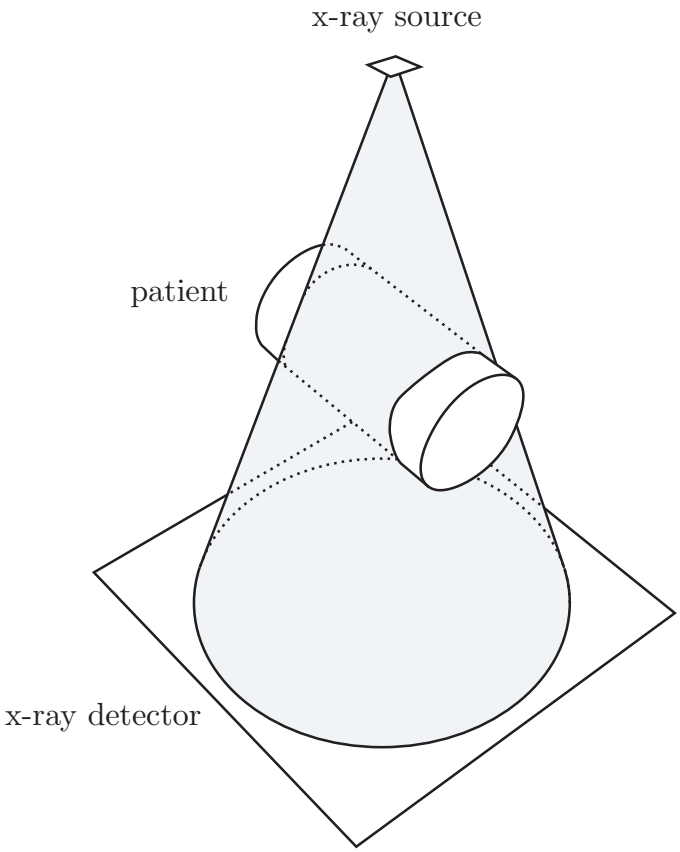

Figure 1.1: A basic representation of a CBCT imaging geometry. The wide-field cone-beam irradiates a large portion of the patient, allowing for a faster imaging procedure for CT techniques.

is the more common of the two, and as such is adopted here as the standard.

Following the acquisition of the projection images, each projection is then filtered, via convolution with a filtering function. [4] Generally, a CBCT filtering function is designed to reduce the lower-frequency portions of the signal to allow use of a back-projection algorithm for the next step, reconstruction. Without a filter, a reconstructed point would have a tapered drop-off instead of a hard edge. More specifically, filters are generally formed so as to correct the point spread function seen when reconstructing a singular point. Without filtration, this point spread function appears similar to an inverse function ($y = 1/x$) rather than the desired δ-function ($y = \delta_x$). The filter used in this work, the Shepp-Logan filter, also includes some additional high-frequency smoothing in order to reduce the noise in the reconstructed images.

The final step in obtaining a CBCT image slice is the reconstruction of the image. The most basic concept of the reconstruction method is the summation of the backprojections of all the filtered slices. This backprojection method projects the filtered values back along the beamlet paths that were used to acquire them. In order to do this, the divergence of the beam also needs to be taken into account.

In previous generations of CT imaging, fan-beam scans were used. In this fan-beam scanning technique a single row detector in conjunction with a much more constrained 'fan-beam' is used. Compared to this, cone-beam CT offers much quicker scan times over a volume, allowing it to be more clinically feasible. However, this speed does not come without a cost. A common artifact CBCT images experience is a 'cupping artifact' caused by the scattered radiation. [5] Compared to fan-beam CT, the beam and detector used are much wider in CBCT, and as such the scattered radiation from the wider beam falling upon any given area of the detector is much larger. This causes a higher than ideal signal to be recorded by the detector in areas with higher scatter signals, causing imperfections in the final image. Fig. 1.2 compares im-

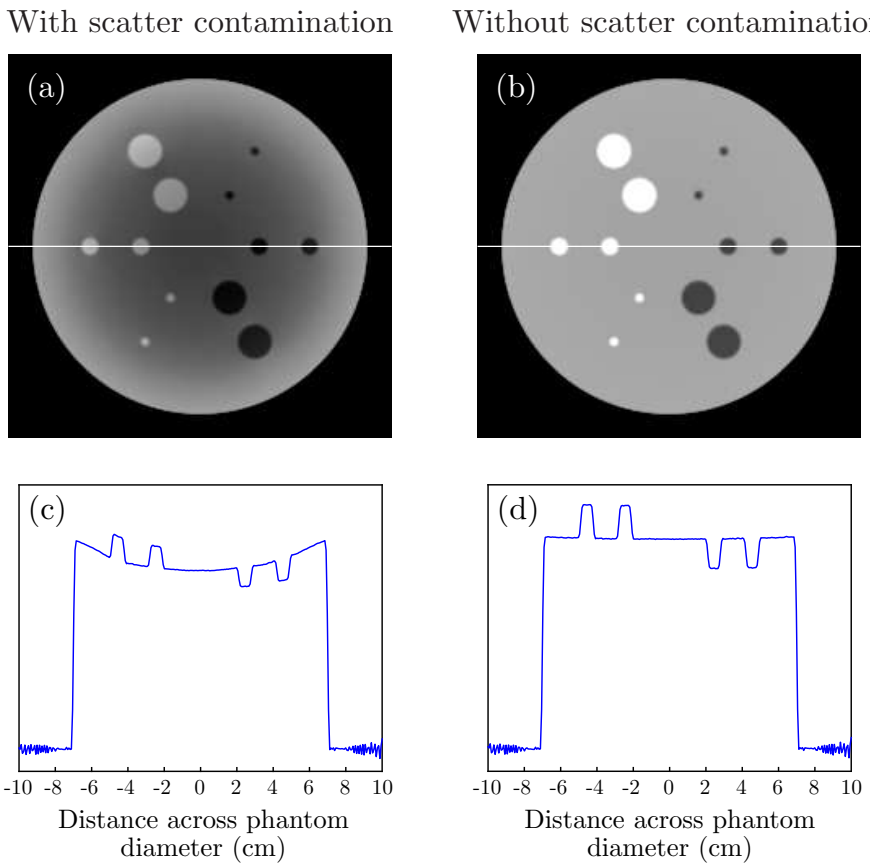

Figure 1.2: A side-by-side comparison of reconstructed images with (a) and without (b) scatter contamination, alongside respective image profiles (c,d). The cupping artifact is clearly visible in the line profile in the form of a decreased reconstructed signal at the phantom center, where the scatter signal is largest. The image profiles are taken along the horizontal white line shown in the reconstructed images.

ages along with image profiles of a simulated phantom for images reconstructed with no scatter contamination against a scenario with scatter. These images were formed with a polyenergetic spectrum and simulation method later described in Chapter 4. The cupping artifact is clearly visible in the profile of the scatter-contaminated image. This artifact can cause difficulty when viewing and interpreting the CBCT images, and as such must be corrected for.

1.2 Literature

Breast cone-beam computed tomography (CBCT) has been in the development stage for over a decade. [6, 7, 8, 9, 2, 10] A higher mammographic density (i.e. higher fibroglandular content) increases the risks of developing breast cancer. [11] Volumetric breast density can be measured by three-dimensional images obtained via breast tomosynthesis [12] or CBCT. [13] Tight clusters of microcalcifications can be an indicator of early breast cancer. CBCT has the potential to improve the characterization of microcalcification patterns [14, 15] and lesions [16] in the breast. Karellas and Vedantham [10] give a good perspective of breast imaging and discuss the potential of dedicated CBCT for breast imaging systems.

Chen *et al.* [17] characterized the scatter fields for CBCT breast imaging tasks using experiments and Monte Carlo simulations. For a 14 cm diameter 10.5 cm long breast epoxy phantom equivalent to a 50:50 mixture of fibrous and fat tissue, a Scatter to Primary Ratio (SPR) as high as 0.5 can occur. [17] Common correction methods use experiments, modeling, Monte Carlo simulations or combinations of these techniques.

Kontson and Jennings [18] analyzed the use of bowtie filters to reduce scatter in breast CBCT projections. They showed reduced peak scatter to primary ratios by approximately 18% and more uniform scatter distributions over a wide range of breast diameters. Sechopoulos [19] developed a scatter correction procedure that requires

an additional set of CBCT projections acquired with an x-ray beam that has been collimated into a number of pencil beams. These latter projections are subtracted from original ones to estimate the scatter components at the locations of the pencil beams. An interpolation scheme provided scatter estimates at other locations. The scatter projections were then subtracted from the CBCT projections. For negligible additional radiation dose, observations obtained with a breast phantom were: reduced cupping artifacts, increased contrast between fatty and glandular equivalents, higher voxel value accuracy, and no discernible blurring of high frequency features.

Cai *et al.* [20] measured the scatter projections for three anthropomorphic uncompressed breast phantoms of different sizes and results indicated that the profiles were mainly determined by local breast diameters. Altunbas *et al.* [21] developed a background non-uniformity correction method to reduce the cupping artifact. Their results obtained with mastectomy specimens showed improved signal uniformity.

1.3 Thesis Outline

The work of this thesis consists of development and testing of x-ray scatter models for use in approximating scatter in CBCT imaging procedures. Commonly Monte Carlo simulation methods are used for this purpose, however this approach tends to be computationally taxing. The models developed in this work aim to be much more computationally quick in order to allow a more in-depth study of scatter effects. A faster simulation time also allows the possibility of a simulation-based scatter correction in a clinical setting.

In order to develop such a model, we begin by looking at the interactions of x rays with matter in Chapter 2. This theory-focused chapter covers the various interactions which need to be understood in order to model x-ray scatter, and concludes with a brief discussion of the interaction probabilities for breast tissue taken from lit-

erature. This is followed by Chapter 3, where this theory is put to use in developing the scattering-point models that this work focuses upon. Two models are presented in this work, one being a more robust model and the other a faster but more assuming model. These models are then tested using the methodology described in Chapter 4. The models will be tested both on their ability to reproduce results comparable to the gold-standard Monte Carlo simulations, as well as on their ability to correct the cupping artifact in reconstructed images. The results of these tests are presented and analyzed in Chapter 5. Chapter 6 contatins a discussion of this work, followed by a summary and conclusions in Chapter 7.

Chapter 2

Physics of X-ray Interactions in Diagnostic Imaging

A common definition of x rays is that of photons of energies above 100 eV, which are produced when a substance is bombarded by high-speed electrons. The manner in which these x-ray photons interact with matter is very well known. One of the most widespread application of x rays is in medical imaging, due to the x-ray photon's ability to penetrate matter in ways that light of visible wavelengths cannot. The photons used in any given medical imaging technique are of an energy range chosen to provide high contrast between the different tissue types of interest while simultaneously minimizing the damage caused to the biological tissue. Commonly, photons energies in the range of 20 to 150 keV are used depending on what the imaging task requires.

In the following six sections the interactions of x rays with matter will be described. First, section 2.1 will outline basic x-ray attenuation through matter. A more specific discussion of the various types of x-ray interaction events will follow in sections 2.2 through 2.5. Section 2.6 will then introduce the related x-ray data corresponding to types of breast tissue which will be used for the simulation work in

this thesis.

2.1 X-ray Attenuation

While x rays are known for their ability to penetrate matter, a fraction of these x-ray photons will interact in various ways within the material. These interactions decrease the number of photons transmitted unaltered through an object. The four main ways that x-ray photons can interact with matter are

- Photoelectric absorption
- Compton scattering
- Rayleigh scattering
- Pair production

Let us consider a narrow, monoenergetic beam of x rays of energy E passing through an object, as pictured in Figure 2.1. The change in the number of photons ($\mathrm{d}N(E,z)$), corresponding to the number of interactions taking place within an infinitesimal thickness $\mathrm{d}z$ of the material is proportional to the number of photons entering this material thickness ($N(E,z)$), such that;

$$\mathrm{d}N(E,z) = -\mu(E)\, N(E,z)\, \mathrm{d}z \tag{2.1}$$

where $\mu(E)$ is referred to as the attenuation coefficient of the material, which is a function of the x-ray photon's energy. This attenuation coefficient is the sum of the probabilities of photon interaction by any of the four previously mentioned interaction types. As such we can write,

$$\mu(E) = \mu_{photo}(E) + \mu_{Comp}(E) + \mu_{Rayl}(E) + \mu_{pair}(E) \tag{2.2}$$

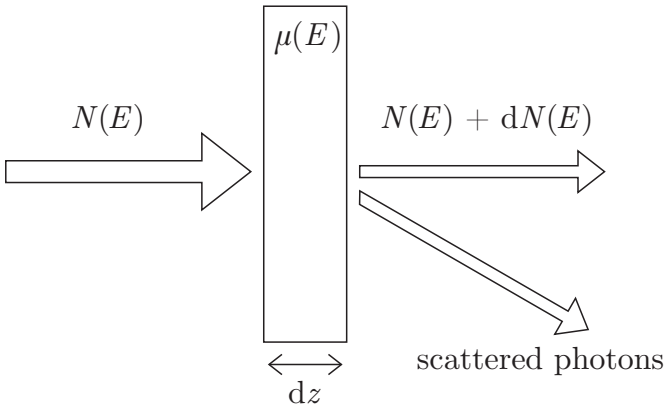

Figure 2.1: A monochromatic x-ray beam consisting of $N(E)$ photons passing though an object of thickness dz with an attenuation coefficient $\mu(E)$. Through interactions within the material, the x-ray beam exits the object with a decreased intensity $N(E)+$ d$N(E)$ photons.

where the summed terms represent the respective probabilities of the various interactions the photons may undergo, as listed previously. The value of μ as well as its component terms are probabilities of interaction per unit length, and thus have units of inverse length.

Integration of equation 2.1 shows that the number of transmitted photons for a given energy through an object of length L, $N(E, L)$, is given by

$$N(E, L) = N(E, 0) + \int_0^L \mathrm{d}N(E, z) = N(E, 0)\, e^{-\int_0^L \mu(E)\, \mathrm{d}z} \tag{2.3}$$

where $N(E, 0)$ represents the number of photons entering the material, and the attenuation coefficient of the material for photon energy E is given by $\mu(E)$. This result is also known as the Beer-Lambert Law.

The mass attenuation coefficient of a material, the ratio of the attenuation coefficient to the material's mass density ρ, can then be calculated as

$$\frac{\mu(E)}{\rho} = \sigma_{tot}(E)\, \frac{N_A}{A} \tag{2.4}$$

where σ_{tot} is the total atomic cross section of interaction at energy E, N_A is Avogadro's number, and A is the atomic mass of the element. In the case of a material made up of multiple elements, the mixture rule allows calculation of the mass attenuation coefficient by assuming these elements are independent of one another. This mixture rule can be stated as

$$\frac{\mu(E)}{\rho} = \frac{\sum_i m_i \left(\frac{\mu(E)}{\rho}\right)_i}{\sum_i m_i} \tag{2.5}$$

where the summations are over the various molecules that make up the material, m_i is the mass fraction and $\left(\frac{\mu(E)}{\rho}\right)_i$ the mass attenuation coefficient of molecule i.

2.2 Photoelectric Absorption

Photoelectric absorption is the process of a photon interacting with one of an atom's bound orbital electrons, as shown in Figure 2.2. In this process the photon is completely absorbed and the electron receives enough kinetic energy to free it from its orbital. This newly freed electron is commonly referred to as a photoelectron. This process can be described by the equation

$$\text{photon} + \text{bound } e^- \rightarrow \text{free } e^- \ (+ E_{kin})$$

As such, for this process to occur, the photon's energy is required to be greater than the binding energy of the electron. Since the photon is completely absorbed in this process, the kinetic energy of the newly freed electron is simply the difference between the photon's initial energy and the binding energy. This can be written as

$$E_{kin} = h\nu - E_B \tag{2.6}$$

where $h\nu$ is the energy of the photon, and E_B is the binding energy of the orbital electron. This energy requirement for the process to occur adds discontinuities in

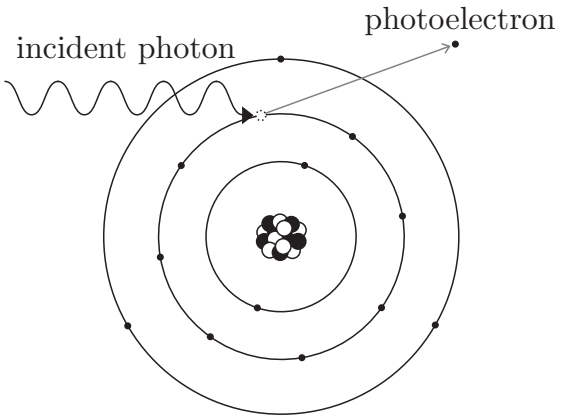

Figure 2.2: A schematic diagram of a photoelectric absorption event. The incident photon's energy frees an orbital electron. Excess energy beyond that required to overcome the binding energy is converted into kinetic energy for this newly freed electron.

interaction probability. These discontinuities exist on energy boundaries where the photon's energy is barely enough to free electrons from an additional orbital shell with a higher binding energy.

By freeing an orbital electron, this process also creates a vacancy in an electron shell. This vacancy, or hole, is quickly filled by either a higher orbital electron or a nearby free electron in the material. The excess energy from this hole-filling transition will either release a new secondary characteristic photon or it may free a second loosely-bound electron from the atom's orbit. This second freed electron is known as an Auger electron, and this may only occur if the transition energy to fill the hole is great enough to overcome this electron's binding energy.

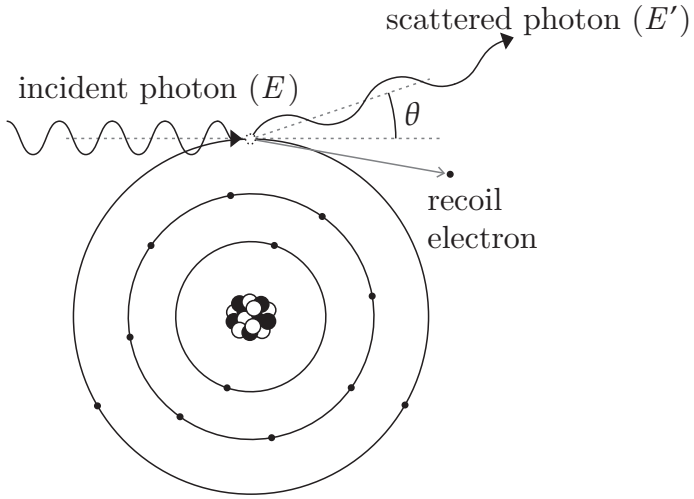

Figure 2.3: A schematic diagram of a Compton scattering event. The incident photon interacts with a quasi-free electron, freeing it at the cost of some of its energy.

2.3 Compton Scatter

Compton scatter, also commonly referred to as incoherent scatter, is a scattering interaction between a photon and quasi-free electron. The quasi-free electron may either be a truly free electron in the material or, more commonly, a loosely bound orbital electron of an atom.

Figure 2.3 illustrates a Compton scattering event. The photon interacts with the electron, ejecting it from the atom, and scattering the photon at an angle θ from its original trajectory. Similar to photoelectric absorption, the electron is quickly reabsorbed into the material. In this interaction the photon transfers some of its initial energy to the electron, freeing it from its orbit and giving it kinetic energy. This process can be shown in the form of the equation

$$\text{photon}(E) + \text{bound e}^- \rightarrow \text{free e}^- \ (+ E_{kin}) + \text{photon}(E')$$

where the photon's resultant energy (E') is lower than its initial energy (E). Under the assumption that the electron has negligible binding energy and initial kinetic

energy, one can use the conservation of energy and momentum to derive this energy shift. The result of this is known as the Compton energy shift equation and is given by,

$$E' = \frac{E}{1 + \frac{E}{m_0 c^2}(1 - \cos(\theta))} \tag{2.7}$$

where $m_0 c^2$ is the rest energy of the electron, 511 keV. For scattering events with a small angular deviation of the photon, little of the photon's initial energy is transferred to the electron. With the energy ranges used in diagnostic imaging, even for the scenario of greatest energy transfer ($\theta = \pi$) the photon retains the majority of its initial energy.

Before discussing the scatter distribution of Compton scatter, we must first introduce classical mechanics scattering; Thomson scattering. The process of Thomson scattering can be described as an interaction between an electromagnetic wave and an electron from an atom of quasi-free electrons. The interaction forces the electrons to vibrate in a manner which then re-emits the electromagnetic wave at a difference angle with the same energy. For an unpolarized incident wave, the differential angular cross section of this classical process is given by

$$\frac{\mathrm{d}\sigma_{\mathrm{Thomson}}}{\mathrm{d}\Omega} = \frac{r_0^2}{2}\left(1 + \cos^2(\theta)\right) \tag{2.8}$$

where r_0 is the classical electron radius, and θ is the angle at which the wave is scattered. This classical derivation assumes that the wave retains its initial energy after scattering, but to model Compton scatter we must take into account that this isn't the case. In order to correct the differential angular cross section, Klein and Nishina used relativistic and quantum mechanics to derive a correction factor. The Klein-Nishina corrected cross section is given by

$$\frac{\mathrm{d}\sigma_{\mathrm{KN}}}{\mathrm{d}\Omega} = \frac{\mathrm{d}\sigma_{\mathrm{Thomson}}}{\mathrm{d}\Omega} \times F_{\mathrm{KN}}(E, \theta) \tag{2.9}$$

where $F_{\mathrm{KN}}(E, \theta)$ is the Klein-Nishina formula. For a photon energy of E and scatter-

ing angle θ, this is given by

$$F_{\mathrm{KN}}(E,\theta) = \frac{1}{\left(1+\alpha\left(1-\cos(\theta)\right)\right)^2} \times \left(1 + \frac{\alpha^2\left(1-\cos(\theta)\right)^2}{\left(1+\alpha\left(1-\cos(\theta)\right)\right)\left(1+\cos^2(\theta)\right)}\right) \quad (2.10)$$

where α is the ratio of the photon's energy to the electron's rest mass, or $\alpha = \frac{E}{m_0 c^2}$. This corrects for energy transfer to the electron, however the effects of the electron's binding energy are still unaccounted for. This is corrected for via use of the incoherent scattering function $S(x)$, where x is the momentum transfer variable, defined as $x = \frac{E}{hc}\sin(\frac{\theta}{2})$. This momentum transfer variable combines the dependence of the scatter probability upon both scattering angle (θ) as well as the photon energy (E). The final differential angular cross section for Compton scatter, corrected for these factors, is thus given by

$$\frac{\mathrm{d}\sigma_{\mathrm{Compton}}}{\mathrm{d}\Omega} = \frac{\mathrm{d}\sigma_{\mathrm{Thomson}}}{\mathrm{d}\Omega} \times F_{\mathrm{KN}}(E,\theta) \times S(x) \quad (2.11)$$

For a material which isn't purely elemental, the atomic form factor S of the material must be either measured or calculated. A common method of calculating the scattering function is known as the Independent Atomic Model (IAM). As its name implies, the IAM assumes that all atoms which make up a material are independent of one another. The calculation using the IAM is given by

$$S_{\mathrm{IAM}}(x) = \sum_i n_i^{\mathrm{Atoms}} S_i(x) \quad (2.12)$$

where the summation is over the elements of the material, and n_i^{Atoms} is the fractional number of atoms of element i in the material.

2.4 Rayleigh Scatter

Rayleigh scatter is an elastic scattering event between a photon and atom. Figure 2.4 illustrates a Rayleigh scattering event. In this event, the photon interacts with the

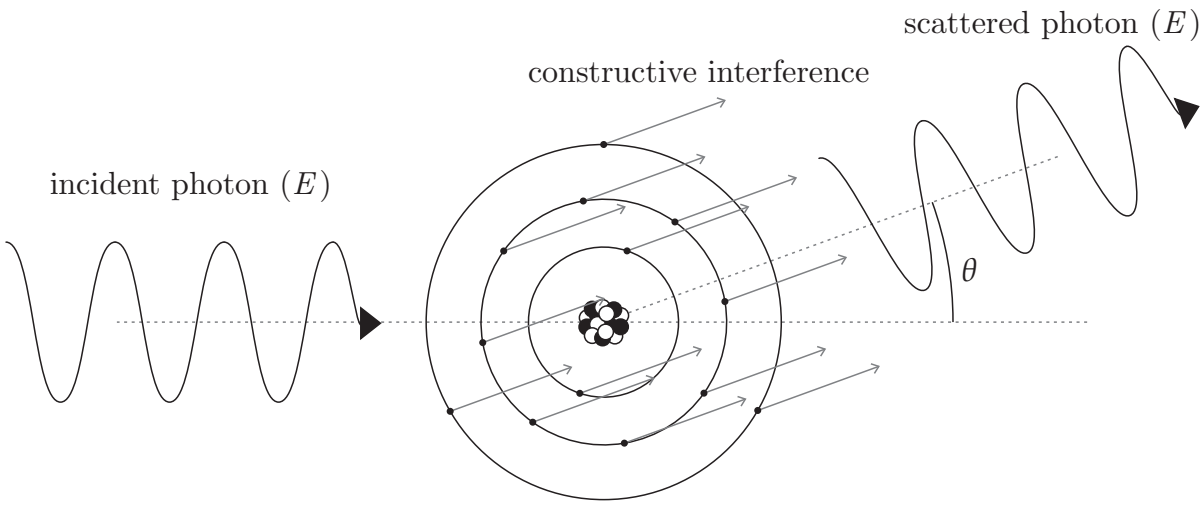

Figure 2.4: A schematic diagram of a x-ray photon undergoing Rayleigh scatter. The photon forces the atom's orbitals to oscillate. These oscillations give rise to an emitted photon of the same energy as the incident photon.

atom's orbital electrons, causing them to briefly vibrate. The electromagnetic field from these vibrations creates constructive interference at a certain angle, which is equivalent to the classically scattered photon. Thus, Rayleigh scatter is also referred to as coherent scatter. This process can be represented by the equation

$$\text{photon}(E) + \text{atom} \rightarrow \text{photon}(E) + \text{atom}$$

As with Compton scattering, we can calculate the energy using an equation similar to Eq 2.7. In this case, however, the interaction can be seen to take place between a photon and the entire atom (instead of an electron). Due to this large mass difference, the energy shift is negligible.

Once again, we can calculate the differential angular cross section by starting with Thomson scattering as in Eq 2.8. To then expand this to multi-electron atoms, it must be corrected to account for the shape of the electron's orbitals and binding energies. This correction factor is known as the atomic form factor $F(x)$, and as such

the corrected differential angular cross section can be written

$$\frac{\mathrm{d}\sigma_{\mathrm{Rayleigh}}}{\mathrm{d}\Omega} = \frac{\mathrm{d}\sigma_{\mathrm{Thomson}}}{\mathrm{d}\Omega} \times F^2(x) \tag{2.13}$$

This coherent scattering function $F(x)$ is dependent upon the arrangement of orbital electrons. As such, for a Rayleigh scattering event between a photon and molecule this form factor is dependent upon the full orbital electron configuration of the molecule. This fact makes the form factor extremely difficult to derive theoretically for even slightly complex molecules. For many materials of interest the form factors $F^2(x)$ have been measured experimentally.

As seen before with Compton scattering, an independent atomic model can be used to calculate the atomic form factor F for a non-elemental material. Similarly to before, this is given by

$$F^2_{\mathrm{IAM}}(x) = \sum_i n_i^{\mathrm{Atoms}} F_i^2(x) \tag{2.14}$$

where the summation is over the elements of the material, and n_i^{Atoms} is the fractional number of atoms of element i in the material. However, unlike with Compton scattering, the IAM is not an accurate approximation for the atomic form factor F. This is due to the fact that for the coherent scattering function (F), the atoms cannot be assumed to be independent since the electron configuration of an atom is altered when under the forces of molecular bonds. This difference in the coherent form factor is a diffraction effect. Figure 2.5 compares the IAM approximation and the experimentally measured coherent scattering functions for both fibrous and fatty breast tissue, along with that of water. The sources of these data will be discussed in more detail in section 2.6. As seen in this figure, the diffraction effects tend to cause a decrease at very low x values, while at high x values the diffraction effects are minimal and the function is well approximated by the IAM. In the range between these effects, diffraction can yield interesting information which can often be used to identify a material.

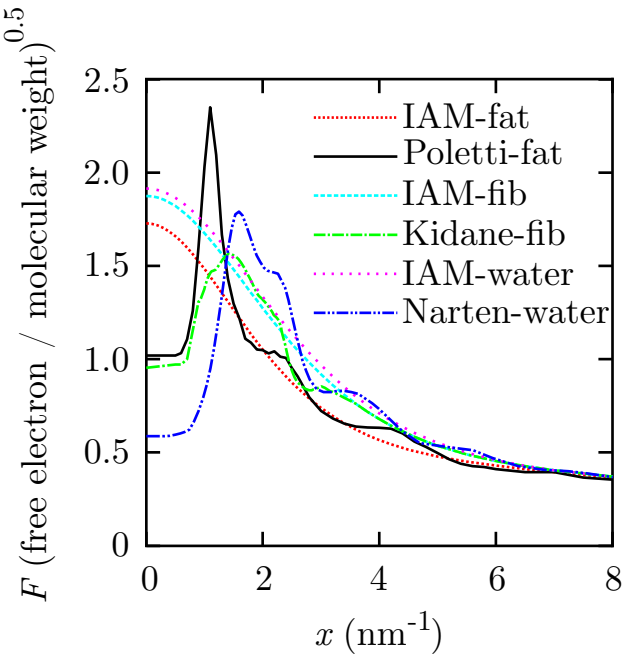

Figure 2.5: Coherent form factor data for breast tissue.

2.5 Pair Production

Pair production is an interaction between a photon and a nucleus' electromagnetic field in which the energy of the photon is converted into an electron and positron pair. This can be represented as

$$\text{photon}(E) \rightarrow \text{e}^- + \text{e}^+ \ (+ E_{kin})$$

From the laws of energy conservation, we know that this event is energetically impossible for photon energies below 1.022 MeV since the rest mass of an electron is 0.511 MeV. Excess energy from the photon above this threshold is split between the initial kinetic energies of the electron and positron. Since this interaction is impossible for x-ray energies used in imaging, it is included here of purely academic interest, but omitted from further mention in this work.

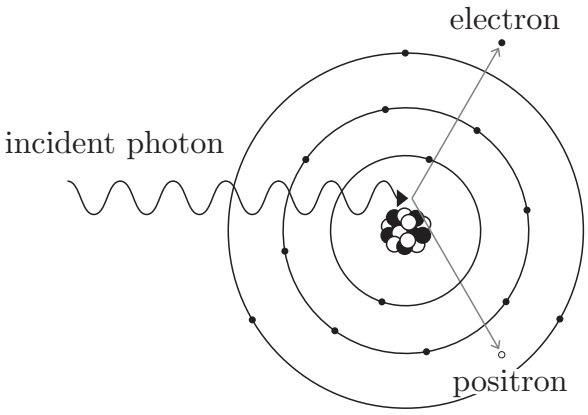

Figure 2.6: A schematic diagram of a photon undergoing pair production. When passing though an atom's Coulomb field, 1.022 MeV of the photon's energy is converted into the mass of the electron/positron pair while the remaining energy becomes kinetic energy for these new particles.

2.6 X-ray Properties of Breast Tissue

The two major types of healthy breast tissue are fibroglandular and fatty tissue. The attenuation coefficients (μ) of fibroglandular (fib) and fatty (fat) breast tissue are shown in Fig. 2.7, along with that of infiltrative ductal carcinoma. These data are those published by Johns and Yaffe [22], and will be used throughout this work. Though the attenuation values for fat are well separated from the other two, the fact that fib and cancer are very similar makes classification of tissue using just transmission values exceptionally difficult. Commonly, images encompassing a suspicious lesion must be manually viewed in order to make a judgment using the appearance of the lesion in the image(s).

Fibroglandular (fib) and fatty (fat) tissue also have very distinctive x-ray diffraction signatures [23, 24, 25] and their coherent scattering functions (F) are shown in Fig. 2.5 as a function of the momentum transfer variable x. The diffraction (Diff) data for fat are those published by Poletti *et al.*[25] and those of fib extracted from Kidane

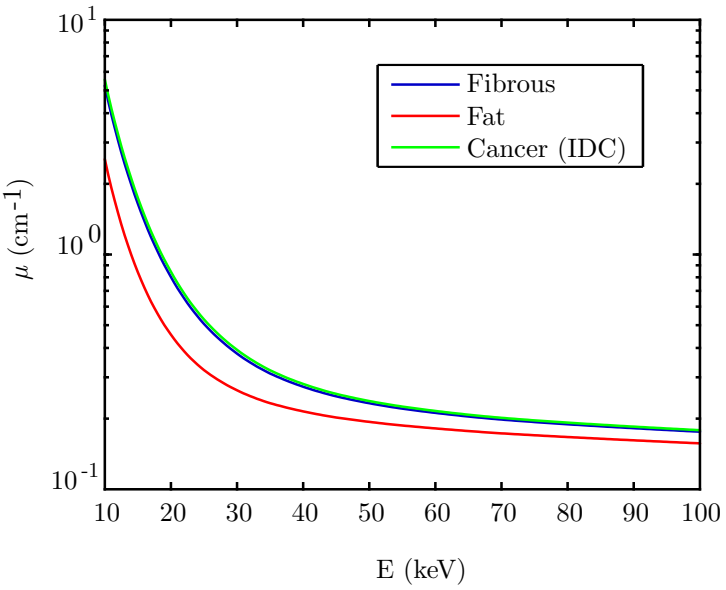

Figure 2.7: Attenuation values of breast tissue.

et al.[24] μ_s data. The latter source of data lacked signals at low $x < 0.8$ nm^{-1} and therefore data were extended to 0 by judging what happens for the case of fat. The F values calculated via the independent atomic model (IAM) approximation are also shown in Fig. 2.5. For higher x, the IAM was used. In order to calculate the IAM approximations, elemental coherent form factors (F) and incoherent scatter functions (S) from Hubbell *et al.*[26] were used in combination with elemental compositions by weight as measured by Hammerstein *et al.*[27] While a number of groups have attempted to measure the scatter signals of breast cancers, the results have lacked strong agreement between them. It is suspected that these disagreements may be caused by the presence of fat in the measured tissue, or the lack of control over the hydration of the sample.

As no reliable measurement of the scatter characteristics of cancerous tissue exists in literature, in this work it was approximated by the scattering characteristics of water, while still using the published attenuation values for cancerous tissue.

The approximation using water is thought to be acceptable due to the increased cell density (majority water) in malignant tissue which is undergoing rapid cell growth & division. The diffraction data used for water are the gold-standard data published by Narten[28]; these F data are shown alongside those of fib and fat in Fig. 2.5.

Chapter 3

X-ray Models

3.1 Scattering Point Models

In order to study the phenomenon of the scattered photons from x-ray interactions, a model is required. From the previous chapter, we can write the full differential linear scattering coefficient as

$$\frac{\mathrm{d}\mu_s}{\mathrm{d}\Omega}(E,\theta) = \rho_e \frac{r_0^2}{2}\left(1+\cos^2(\theta)\right)\left[F^2(x) + F_{\mathrm{KN}}(E,\theta)S(x)\right] \tag{3.1}$$

which combines the probabilities of scattering via Rayleigh or Compton interactions. ρ_e is the volumetric electron density of the material, r_0 is the classical electron radius, θ is the scattering angle, and the values of $F^2(x)$ and $S(x)$ are the respective scattering functions with dimensions of inverse electrons. This $\frac{\mathrm{d}\mu_s}{\mathrm{d}\Omega}$ probability has dimensions of inverse length by inverse solid angle, or commonly in units of $\mathrm{cm}^{-1}\,\mathrm{sr}^{-1}$.

Consider a scenario where a pencil beam of x-ray photons passes through an object of thickness d where a detector positioned at angle θ collects the scattered photons, as shown in Fig. 3.1. Using this scattering coefficient, an equation for the number of scattered photons reaching the detector can then be derived. Under the

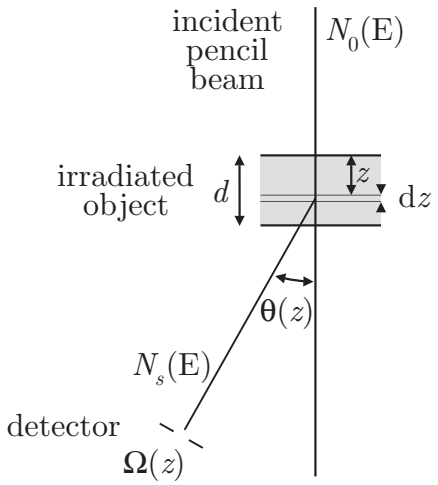

Figure 3.1: A schematic of the scattering from a beamlet passing through an object.

assumption that the Compton energy shift is negligible for the energies and angles we're interested in, the following equation can be obtained;

$$N_s(E) = \int_0^d N_0(E)\, e^{-\mu(E)z} \int^{\Omega(z)} \frac{\mathrm{d}\mu_s}{\mathrm{d}\Omega}(E, \theta(z))\; e^{-\mu(E)\frac{(d-z)}{\cos(\theta(z))}}\, \mathrm{d}\Omega\, \mathrm{d}z \tag{3.2}$$

where the outer integration is over the thickness of the object the photon beam is passing through, and the inner integration is over the sensitive area of the detector. The factor $e^{-\mu(E)z}$ accounts for attenuation of the photon beam before it reaches layer dz, while the factor $e^{-\mu(E)\frac{(d-z)}{\cos(\theta(z))}}$ accounts for attenuation of the photons after scattering from layer dz. This post-scatter attenuation distance is calculated assuming the object has an exit plane parallel to the detector and perpendicular to the incident beamlet. While this approximation may not be accurate for our later purposes, it is acceptable for now so long as the context is kept in mind. Since the detector distance is usually fairly large compared to the size of the detector pixel area, the simplification can be made that the scattering angle from layer dz is relatively constant over the area of the detector. Thusly, the equation simplifies to

$$N_s(E) = N_0(E)\, \Omega_{\mathrm{det}} \int_0^d \frac{\mathrm{d}\mu_s}{\mathrm{d}\Omega}(E, \theta)\; e^{-\mu(E)z}\; e^{-\mu(E)\frac{(d-z)}{\cos(\theta(z))}}\, \mathrm{d}z \tag{3.3}$$

where Ω_{det} is the solid angle subtended by the detector from any point along the beamlet.

By introducing an average attenuation length that the scattered photons see ($\overline{l_{exit}}$) we can remove the $e^{-\mu(E)\frac{(d-z)}{\cos(\theta(z))}}$ factor from the integral and have this derivation apply to a more general scenario. Doing this, one can integrate the rest of this equation to yield the total scatter from an object

$$N_s(E) = N_0(E)\,\frac{\mathrm{d}\mu_s}{\mathrm{d}\Omega}(E,\theta)\,\frac{\Omega_{\text{det}}}{\mu(E)}\,e^{-\mu(E)\,\overline{l_{exit}}}\,(1-e^{-\mu(E)d}) \tag{3.4}$$

In this simplified equation, by keeping in mind the context through the derivation, some significance can be applied to the individual factors. The factor $N_0(E)\,(1-e^{-\mu(E)d})$ is the number of interactions occurring through the beamlet's length in the material; while the factor $e^{-\mu(E)\,\overline{l_{exit}}}$ is related to the attenuation of the photons by the material after scattering.

3.1.1 Many Scattering Point Model

Our intention, however, is to model the scatter during cone-beam CT. In order to create a simple model of CBCT scatter, the factors of equation 3.4 can be adjusted to fit the context of a CBCT measurement. Firstly, in order to simplify the diverging x-ray cone shaped beam, it is conceptually broken down into a number of individual pencil beam (or beamlets). For simplicity, the cone-beam will be divided into beamlets such that each detector pixel has exactly one primary beamlet incident upon its center. Additionally, each beamlet will be segmented into smaller sections within the phantom in order to better adhere to the assumptions made in deriving Eq 3.4 when brought to CBCT geometries. The second modification of this equation needed is to the factor relating to the post-scatter attenuation. For an arbitrarily shaped phantom, a more rigorous line-shape intersection method is necessary. In this work,

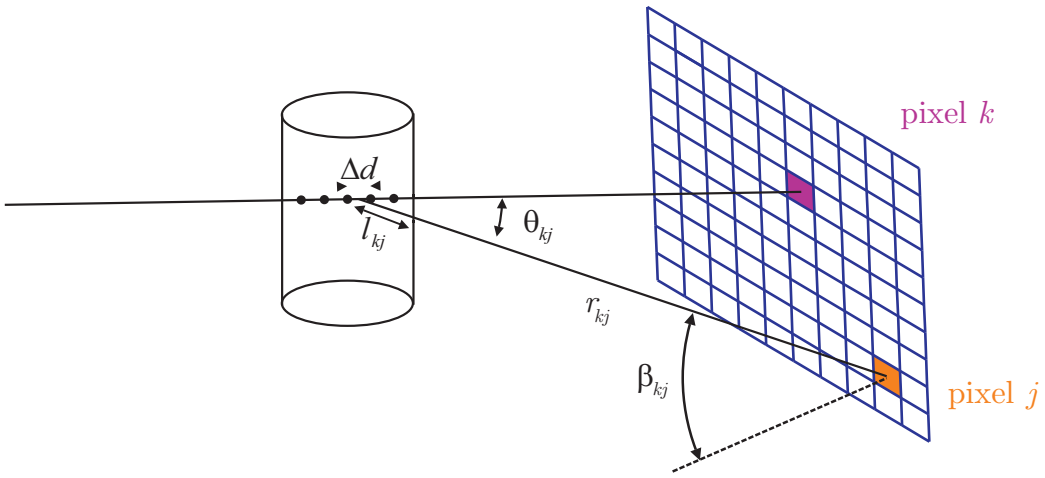

Figure 3.2: A schematic of the Many Scattering Point model approximation in a CBCT geometry.

however, the phantoms used are simple cylinders which helps alleviate complexities in this calculation. With these changes, for a geometry as shown before in Fig. 3.2, the scatter incident upon pixel i from a beamlet k can be modeled through the equation

$$N_s^{k,j}(E) = \sum_m N_0(E)\, e^{-\sum_n \mu_n(E)\Delta d_n}\, (1 - e^{-\mu(E)\,\Delta d_m})\, \frac{d\mu_s}{d\Omega}(E, \theta_{kj:m})\, \frac{\Omega_{kj:m}}{\mu(E)}\, e^{-\sum_i \mu_i(E) l_{kj:mi}} \tag{3.5}$$

where the summation m is over the segments which compose this beamlet segment within the phantom. The factor $N_0(E)\, e^{-\sum_n \mu_n(E)\Delta d_n}$ is the number of photons which reach a given beamlet segment after attenuating through any material (n) along the beamlet, $(1 - e^{-\mu(E)\,\Delta d_m})$ is the fractional number of interactions occurring within the beamlet segment m, $\Omega_{kj:m}$ is the solid angle subtended by the detector pixel j from the scattering point m along beamlet k, which is approximated by $\Omega_{kj:m} = A_{pixel}\, {\cos(\beta_{kj:m})}/{r^2_{kj:m}}$, and the factor $e^{-\sum_e \mu_e(E) l_{kj:mi}}$ is post-scatter transmission though any materials (i) the scattered photons pass to reach detector pixel j. All calculations of $\theta_{kj:m}$, $\Omega_{kj:m}$, and $l_{kj:mi}$ use the point at the center of the beamlet segment as the singular point of scattering for segment m. By calculating this model equation for

each of these beamlet segments, the total scatter from the phantom volume to any point upon the detector can be approximated. As this model relies upon using many scattering points along each beamlet, it will be referred to as the Many Scattering Point (MSP) model. For all MSP simulations in this work, the beamlets are segmented such as to guarantee at least one scattering point per 1 cm length of beamlet length within the phantom. This segmentation is also performed as to force a segment end upon material transitions, and as such each beamlet segment only occupies a single material. The implementation of this MSP model in C++, which was used in this work, can be read in Appendix A.

3.1.2 Single Scattering Point Model

While this MSP model closely follows the assumptions made in the derivation of Eq 3.4 and should yield a good approximation of the scatter, it is computationally time consuming to perform the number of calculations needed. As such, a more simplified Single Scattering Point (SSP) model is now proposed. This model incorporates only a single point of scattering per beamlet, meaning that to simulate the scatter signal upon a pixel the summation in Eq 3.5 would only have a single term to calculate per beamlet. Because of this fairly extreme simplification, it is not expected that this model could accurately approximate the scatter profile on the detector as it is. In order to attempt to advance this model, the scattering point will be considered variable along the beamlet length. The scattering points will be the same fractional distance along the beamlet's intersection with the phantom for all beamlets. The variable δ will correspond to the fractional distance into the phantom the scattering point is positioned at; a δ of 0 would represent the upper phantom surface, while a δ of 0.5 would be at the center of the beamlet's length within the phantom. The aim is to have the SSP model yield correct scatter approximations through adjustments of this δ value.

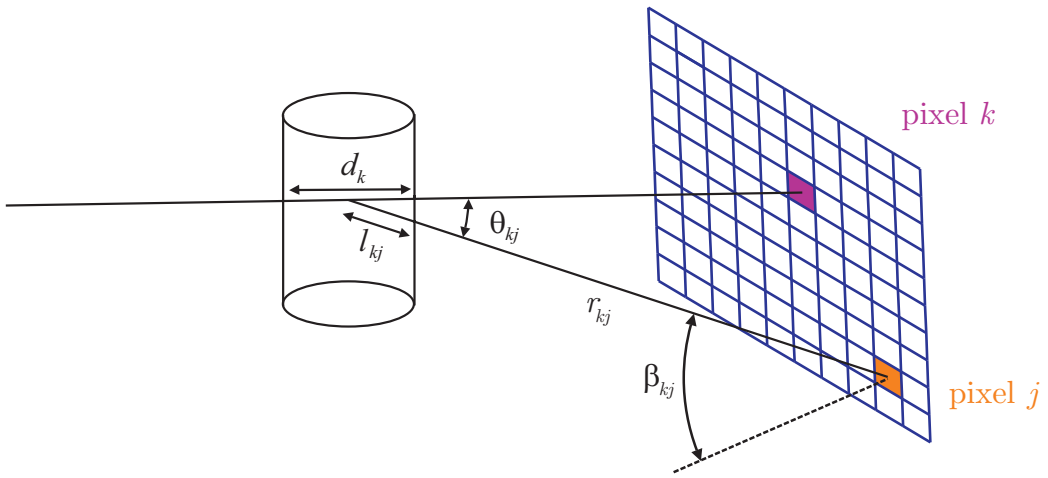

Figure 3.3: A schematic of the Single Scattering Point model approximation in a CBCT geometry.

This SSP model calculation for a beamlet shown in Fig. 3.3 is given by

$$N_s^{k,j}(E) = N_0(E)\,(1 - e^{-\mu(E)\,d})\frac{d\mu_s}{d\Omega}(E, \theta_{kj}(\delta))\,\frac{\Omega_{kj}(\delta)}{\mu(E)}\,e^{-\mu(E) l_{kj}(\delta)} \tag{3.6}$$

where the factors are similarly defined to those of Eq 3.5. The major differences are that the factor $(1 - e^{-\mu(E)\,d})$ accounts for all interactions within the entire beamlet in the phantom, and that the quantities $\theta_{kj}(\delta)$, $\Omega_{kj}(\delta)$, and $l_{kj}(\delta)$ are calculated only once per beamlet for any given δ value.

It may be noted that since these models began from the Compton and Rayleigh singly scattered photons, they do not incorporate any photons which undergo multiple scatter. In cone-beam CT imaging procedures multiple scatter may account for upwards of 50% of the total scatter signal. However, as will be shown in the Results, the multiple scatter tends to have a more featureless and smooth profile over the detector compared to the single scatter. This means that the multiple scatter is easier to approximate, and also tends to have less impact upon the final reconstructed image.

3.2 Geant4 Monte Carlo Model

While the equations governing the interaction probabilities of x rays with matter are well known, they are too complex to yield general analytic solutions. As such, the preferred method of simulating x-ray interactions is to use Monte Carlo methods. In general, Monte Carlo methods make use of random sampling in order to approach the probabilistic result of a situation. More specific to the context of simulating x-ray transmission through matter, this means simulating the paths of a large number of individual photons. Each photon is simulated from its point of creation (the x-ray tube, for our purposes) until its path ends either by absorption, interaction with the detector, or by leaving the simulated world volume. As a photon passes through a virtual material, its path is considered in a large number of discrete steps. Over each of these steps, the probability of interaction (via the various interaction processes described in Ch 2) is sampled using random numbers, and a single 'history' of the photon's path is generated. This history contains information on the material boundaries the photon passed through, the interactions it underwent, and its energy at any of these events. The histories of all simulated photons can then be analyzed en masse in order to obtain information on the dose distribution within the simulated object (for treatment planning) or the distribution of photons leaving the object (for imaging simulations). Only by simulating a large number of photon histories can an accurate solution be approached.

A very commonly used Monte Carlo simulation toolkit is that of Geant4. Geant4 is the latest version of the Geant series of simulation software originally developed by CERN. For this latest version of Geant, the development has moved beyond CERN and is now handled by the Geant4 Collaboration; an international collaboration of scientists and software engineers dedicated to developing, maintaining, and providing support for Geant4. The Geant4 toolkit is programmed in C++ with an object-

oriented design and allows construction of a desired world geometry using binary operations of simple volumes. The simulation of electromagnetic processes do not have strict energy limits; while the default data provided are of the range of 100 eV to 100 TeV, numerous packages have been made available reflecting various group's measurements of other energy ranges.

Chapter 4

Methodology

In this chapter the methodology of the thesis work will be described along with motivations. First, a general overview of the simulation geometry, spectrum, and detector is given. Following this, a validation of the two scattering point models' abilities to approximate scatter in CBCT imaging tasks is presented using a mainly homogeneous phantom. Following this initial validation, the SSP model is more thoroughly tested for its ability to correct for scatter in reconstructed images of a phantom with large inhomogeneities.

4.1 Simulation Geometry

In order to test the scattering point models, two cylindrical phantom designs were simulated. The simulated geometry was that of a 1.5× magnification CBCT scan, with a point source to phantom isocenter distance of 58 cm and a source to detector distance of 86 cm. The phantom materials simulated were various mixtures of fibroglandular (fib) and fatty (fat) tissue. The two phantom designs used are shown in Fig 4.1. The phantom design A had a diameter of either 7 or 14 cm, an axial length of 10.5 cm, and contained three thin groups of axial cylinders with diameters

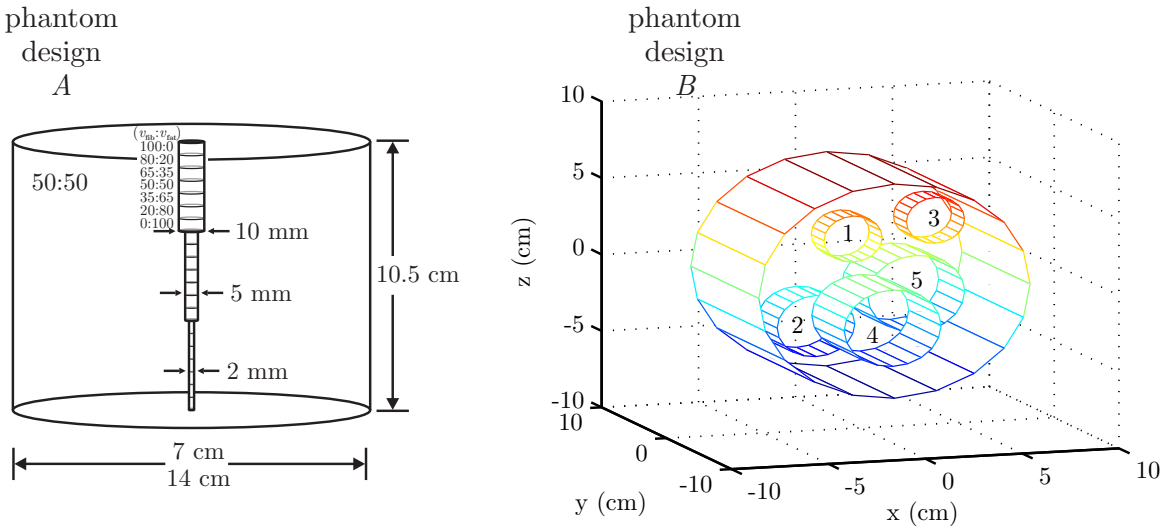

Figure 4.1: Schematics of cylindrical phantoms simulated. Details of phantom design B's substructure are included in Table 4.1.

Cylinder #	length (cm)	diameter (cm)	r (cm)	θ (°)	ϕ (°)
1	2	3	3	45	90
2	3	4	5	135	120
3	2	3	5	45	0
4	5	5	3.5	135	270
5	4	5	5	110	45

Table 4.1: Specifications for the 5 embedded cylinders of phantom design B.

of 2, 5, and 10 mm. While the main phantom body had a m_{fat}:m_{fib} composition of 50%:50%, each of the embedded cylinder groups consisted of cylinders with sequential compositions of; 100:0, 80:20, 65:35, 50:50, 35:65, 20:80, 0:100. The other phantom design B was 14 cm in diameter with a 10.5 cm axial length, and contained five large cylindrical segments designed to introduce heterogeneity. The specifications of these embedded cylinders are recorded in Table 4.1. These cylinders occupied 15% of the total phantom volume. Two compositions of main phantom and embedded cylinders were chosen to reflect two different BIRADS [29] groups; one with a breast density of 85% volumetric fib, and another for 15%. The first configuration consisted of having the main phantom cylinder modeled as fibroglandular tissue, with the inner cylinders modeled as breast fat. The second configuration was the opposite of the first, with the main cylinder consisting of fat, while the inner cylinders of fib. The overall mass fractions of these configurations were $m_{\text{fib}} = 86.4\%$:$m_{\text{fat}} = 13.6\%$, and 16.5:83.5 respectively.

The simulated detector had dimensions of 30 cm $\times$ 30 cm with energy integrating pixels. An ideal detective quantum efficiency of unity was assumed. The x-ray spectrum used in this work, shown in Figure 4.2, was that of a 60 kV beam from a tungsten anode with a HVL of 3.7 mm Al, originating from a spectral catalog published by Birch *et al.* [30]. Since the aim of the first section (Sec. 4.2) of this work is to analyze the scatter profiles, and not necessarily the reconstructed images, only a single rotation needs to be simulated. While in a later section (Sec. 4.3) reconstructed images are used, so the fluence shown in Fig. 4.2 was divided amongst the 300 projections, for Section 4.2 the entirety of the shown spectrum was simulated upon a single projection. For all simulations of phantom design A, the detector was made up of pixels of 1 mm^2, yielding a detector consisting of 300 pixels per side. For the phantom design B, which required more calculations regarding beamlet-volume intersection, the pixels were 3mm^2, yielding a 100 $\times$ 100 detector. This change to

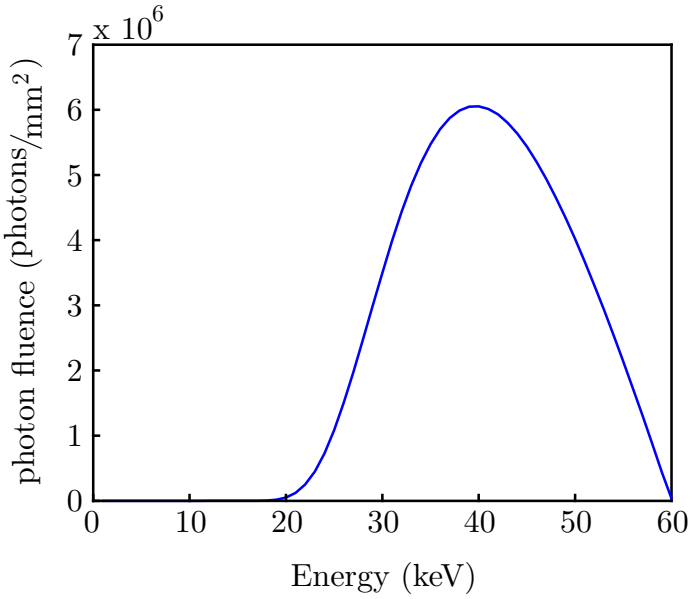

Figure 4.2: The total photon fluence upon the detector over 300 CBCT projections.

a lower resolution increased simulation speeds for MSP model calculations and was made without sacrificing data of interest, since the results concerning phantom B are purely based on the reconstructed image profiles.

The Energy Integrated Signal (EIS) upon any given detector pixel (i) was simply calculated by

$$EIS_i = \sum_n N_i(E_n)\, E_n \tag{4.1}$$

where the summation is over the range of energies in the spectrum, and $N_i(E_n)$ is the number of photons incident upon detector pixel i of energy E_n. To compare the scatter results, a scatter to primary ratio (SPR) for each pixel i was calculated via

$$SPR_i = \frac{EIS_{i:s}}{EIS_{i:p}} \tag{4.2}$$

where $EIS_{i:s}$ and $EIS_{i:p}$ are respectively the scattered and primary EIS on pixel i. The superscript of the SPR variable will relate it to its method of calculation (ie SPR^{G4} is the SPR as simulated by Geant4).

4.2 Validation of Scattering Point Models

The validation of the scattering point models was performed using the two diameters of phantom design A (shown in Fig. 4.1). All work towards validation is only concerned with the recreating accurate scatter profiles, and as such only single projections were simulated. As mentioned before, since only a single projection was required, and phantom design A was used, the detector consisted of 300×300, 1 mm^2 EIS pixels.

4.2.1 Geant4 Simulations

In this work the Geant4 toolkit is used as a baseline for comparisons, in lieu of physical experiments. In order to simulate breast tissue, this work used the compositions by weight for human tissue as measured by Hammerstein et al. [27]. The Geant4 simulations used the low energy Livermore physics model package [31]. All scatter and attenuation effects due to air were neglected. To acquire acceptable statistics, 38400 photons were simulated heading to each of the pixels for each 1 keV energy bin between 20 and 60 keV. In order to simplify the simulation, the photon fluence upon each detector pixel was assumed to be identical, ignoring the inverse square law and differences in the solid angle subtended by the pixels. This uniform distribution of photon energies was simulated in order to allow application of any desired spectrum as a post-simulation step.

Due to the requirement of simulating a large number of photon histories in order to gather acceptable statistics, a parallelized computing approach was used in this work. Since the individual photon paths can be assumed to be independent of each other, the total number of simulated photons can easily be divided amongst a number of simulating computers running in parallel. In order to do this, the Geant4 code was integrated with a simple Message Passing Interface (MPI) to distribute the simulation tasks amongst the available computers. The Shared Hierarchical Aca-

demic Computing Network (SHARCNET) [32] provided access to the computational facilities necessary to perform these parallel simulations in a reasonable time span.

Following the simulation on SHARCNET, a perl script was applied to analyze the Geant4 output and generate corresponding energy integrated signals (EIS^{G4}) upon the detector pixels. First, as a uniform spectrum was initially simulated, in order to apply the spectrum mentioned previously the final photon counts were simply scaled depending upon the photon's initial energies. This scaling has the additional benefit of reducing variance in the spectral photon counts. Following that, the total energy of the photons incident upon each detector pixel was calculated, yielding the EIS values. Four categories of EIS were calculated, separated across the photon histories: No Interaction (Transmission), Rayleigh scatter, Compton scatter, and Multiple scatter. The Multiple scatter signal consisted of any photons which underwent multiple scattering events; there was no attention given to which scattering event types the multiply scattered photons underwent.

From the categorization mentioned above, SPR profiles were calculated for total scatter, single Rayleigh, single Compton, as well as multiple scatter contributions. In order to further reduce the variance for analysis, the SPR^{G4} values of each pixel was taken as the average of the surrounding 11×11 pixel area.

4.2.2 MSP Model

In order to match with the simulations performed by Geant4, data using the IAM approximation were used in these simulations. The generation of these data was discussed in section 2.6. Rather than the published μ data, new IAM attenuation data were generated using the cross section data from Plechaty *et al.*[33] in conjunction with the mixture rule.

By separating Eq 3.1 between Rayleigh ($F^2(x)$) and Compton ($F_{\mathrm{KN}}(E,\theta)S(x)$)

components, the scatter contributions from these interactions can be calculated separately using the same modeling techniques. Doing this, the model will be tested for how well it matches the Geant4 simulation results for these two scattering interactions independently, as well as in total. Validation was performed by comparing these SPR from the MSP model to those of Geant4.

4.2.3 SSP Model

As mentioned in section 3.1, the scattering point of the SSP model is considered variable along the length of the beamlet intersection with the phantom. The aim of this section is to attempt to identify a δ value which allows the SSP model to correctly calculate the scatter profile upon the detector. The phantoms used here were homogeneous phantoms, matching the overall composition (50:50) of phantom design A while omitting the cylindrical axial substructures; All other phantom and geometry factors were identical to those used previously for the MSP model. Using phantoms matching the overall composition of each of the two phantoms simulated by Geant4, the SSP model is run using various δ values from 0 to 1 in steps of 0.1. Through fitting a curve to the peak SPR values obtained from these SSP runs, and comparing with those via obtained Geant4, this section aims to find the correct δ values which allow reproduction of either the single scatter or total scatter signals.

Following this, in order to extend the SSP model past the Geant4 results, the MSP model is now used as a comparator. The MSP model is used to simulate a number of phantom compositions ranging from 0%:100% to 100:0 in steps of 10% for both the 7 cm and 14 cm homogeneous phantoms. For each of these compositions, the SSP is again run using various δ values from 0 to 1 in steps of 0.1 for each corresponding phantom compositions. Through comparing the MSP simulated peak SPR values to those of the SSP, a function yielding correct δ values for any phantom

composition can be found for each of the phantom diameters. Furthermore, this process is repeated using both IAM scattering functions as well as diffraction data.

4.3 Potential Use of the SSP Model

After testing the SSP and MSP models with a simple, mainly homogeneous phantom using Geant4, the goal of this section is to show the model's ability to correct for the cupping artifact caused by scattering on the reconstructed image, rather than simply reproduce the SPR of a single projection. In this section both phantom designs A (14 cm) and B are used in order to test the model. Because this section requires reconstruction, the MSP model is used as the baseline for the single scatter signals; It would be difficult to use Geant4 to generate the number of projections necessary for reconstruction due to the large amount of computational time which would be required.

For the image analysis with the 14 cm diameter phantom design A (containing 21 embedded axial cylinders) the MSP model generated noiseless projections of EIS_p and EIS_s due to single scatter were used. A fit to the Geant4 EIS_s projection due to multiple scatter (EIS_{ms}) was performed to acquire a smooth profile. The sum of these three signals yielded the total signal $EIS_t = EIS_p + EIS_s^{MSP} + EIS_{ms}^{G4}$, which was assumed to be the signal obtained during an acquisition with no noise. The σ in EIS_t was approximated by

$$\sigma_{EIS_t} = \sqrt{\sigma^2_{EIS_p} + \sigma^2_{EIS_s^{MSP}} + \sigma^2_{EIS_{ms}^{G4}}} \tag{4.3}$$

where

$$\sigma^2_{EIS_p} = \sum_i E_i^2 N_p(E_i), \qquad \sigma^2_{EIS_s} = \sum_i E_i^2 N_s(E_i) \tag{4.4}$$

and $\sigma_{EIS_{ms}}$ was simply taken to be the same as σ_{EIS_s}. Gaussian signals of EIS_t for

any given pixel j were generated for each rotation via

$$EIS_{t:j}^{\text{Gauss}}(E) = randn \times \sigma_{EIS_{t:j}} + EIS_{t:j} \tag{4.5}$$

where $randn$ is a pseudorandom scalar drawn from the standard normal distribution.

For the image analysis with the 14 cm diameter phantom design B (containing the 5 large heterogeneities) a similar procedure was performed, with the main difference of excluding the signal due to multiple scatter. This was done since there was no feasible way to generate multiple scatter profiles for 300 projections using Geant4 in a scenario where the phantom lacks rotational symmetry. For both scenarios, the SSP model is then used to simulate a phantom with a matching overall composition, but lacking in any structural detail. This SSP model calculation used the δ values corresponding to the composition, as found earlier in section 4.2.3.

With these model results, three image sets were reconstructed for each phantom. The first image set corresponds to the ideal scenario of a primary transmission image from the beamlet model. It is the goal of the scatter correction procedure to be able to reproduce images matching these of this ideal scenario. The second image set is that of the scatter contaminated images (as simulated using the MSP model) corresponding to theoretical experimental images. The third and final image set is that of the scatter-corrected scenario, where the SSP model's estimated scatter profile is subtracted from that of the second scenario. The EIS upon any given pixel of each of these scenarios is respectively given as follows

$$EIS_p = EIS_{primary}$$

$$EIS_t = EIS_p + EIS_s^{MSP}$$

$$EIS_{t-s} = EIS_t - EIS_s^{SSP}$$

Using these three signals, the image sets were reconstructed as will now be described.

While the general process of CBCT reconstruction has been covered in the Introduction, the more specific details of the methodology used to reconstruct the images will be covered here. Following the production of the EIS signals via simulation, the first step in processing these signals is to apply a beam hardening correction. This is necessary due to the fact that a multi-chromatic x-ray beam's energies are not attenuated at the same rate as they pass through a material; the lower energy photons will be attenuated much more quickly than those of the higher energies. This effect introduces non-linearity into the standard definition of the radon transform $[\lambda(\theta) = ln(^{N_0}/_{N_p(\theta)})]$. As such, a calibrated hardening function (H) is instead applied to produce the radon transform;

$$\lambda(\theta) = H^{-1}(^{EIS_0}/_{EIS(\theta)}) \tag{4.6}$$

where $H^{-1}()$ is the inverse of the hardening function, EIS_0 is the primary energy integrated signal (such as would be obtained from an image acquisition without an object), while $EIS(\theta)$ is the signal obtained via the image acquisition at projection angle θ. For the purposes of this work, $EIS(\theta)$ in the above equation will be one of the previously defined signals EIS_p, EIS_t, or EIS_{t-s}. The hardening function H is a calibrated signal using the same geometry and spectrum, with a phantom having similar properties to the object the corrective function will be used for. The function is defined as

$$H(d_k) = ln(^{EIS_0}/_{EIS(d_k)}) \tag{4.7}$$

where the hardening function is calibrated across a number of material thicknesses d_k, and $^{EIS_0}/_{EIS(d_k)}$ is the energy integrated signal fraction obtained though material thickness d_k. By fitting this function using a range of thickness values, a nearly linear response can be obtained from Eq 4.6 for materials similar to the one used during calibration.

Following this beam hardening correction, this signal is then prepared for re-

construction via filtering using a discrete Shepp-Logan kernel. The filter application is done using a real-space convolution,

$$P(x, y, \theta) = \lambda(x, y, \theta) *_y f(y) \tag{4.8}$$

where $f(y)$ is the filtering function (i.e. the Shepp-Logan filter in this work), and $P(x, y, \theta)$ is the filtered projection for angle θ.

Using these filtered projections, the reconstructed images are then formed using a FDK backprojection algorithm written for Matlab taken from Ref. [34]. The FDK algorithm [4] is based upon extending a simple fan-beam reconstruction for use in cone-beam imaging. As such, this algorithm tends to produce errors for distant off-central slices relating to the divergence of the beam. Additionally, this algorithm tends to be rather slow for full reconstructions in clinical use. Nonetheless, as the FDK backprojection algorithm is commonly used in CBCT scanners as the standard reconstruction algorithm it was judged as the best method of evaluation in this work. While the referenced FDK algorithm Matlab code did provide an implementation of the Shepp-Logan filter, for this work this filtration was instead performed as a separate step in C++. This was done due to the lack of precision in Matlab's implementation of the Fourier transform. The application of the filter takes approximately 5 min for 300 projections, while the FDK backprojection reconstruction takes approximately 30 seconds per reconstructed image slice. As these are computation times are deemed reasonable, both the application of the filter and the FDK reconstruction are performed on a single local computer.

The final step in preparing these reconstructed images for analysis is the application of Hounsfield units in order to give the reconstructed voxel's values a standardized scale. The Hounsfield Unit (HU) scale is defined as

$$HU(i) = 1000 \times \frac{\mu(i) - \mu_{\text{water}}}{\mu_{\text{water}} - \mu_{\text{air}}} \tag{4.9}$$

where $\mu(i)$ is the reconstructed coefficient of absorption for a given voxel i, and similarly μ_{water} and μ_{air} are the reconstructed values for water and air obtained using the same geometry and spectrum. As such, in order to generate these Hounsfield units a calibration needs to be performed using a phantom containing volumes of water and air, respectively corresponding to $HU = 0$ and $HU = -1000$. This calibration simulation in this work used volumes of air and water embedded in a phantom volume of equal masses fib and fat; with geometry, spectrum, and detector as described previously. With the voxel values obtained from these volumes after reconstruction, a linear fit conversion for image voxel values to HU can then easily performed for other images obtained under the same conditions.

Chapter 5

Results

5.1 Validation of Scattering Point Models

5.1.1 MSP versus Geant4

Figure 5.1 shows the SPR of the central slice across the phantom diameter as calculated by Geant4 for the (a) 7 cm and (b) 14 cm diameter cylinders. The SPRs for the coherent (coh), incoherent (inc), multiple (mult), single, and total scatter components are shown separately. The SPRs obtained with the 14 cm cylinder were much higher than those from the 7 cm phantom. The coherent scatter component of the SPR was larger than the incoherent and multiple scatter components for both phantom diameters. The multiple scatter SPR was larger than that of the single Compton scatter for the 14 cm thick phantom.

The Geant4 single scatter SPR for the 14 cm diameter phantom was compared to the one obtained using the MSP model. The model single scatter data, represented by symbols in Fig. 5.1(b), matched the Geant4 data nicely even though the model calculations were done using a homogeneous $m_{\text{fib}} = m_{\text{fat}} = 50\%$ phantom, omitting the substructures along the phantom axis.

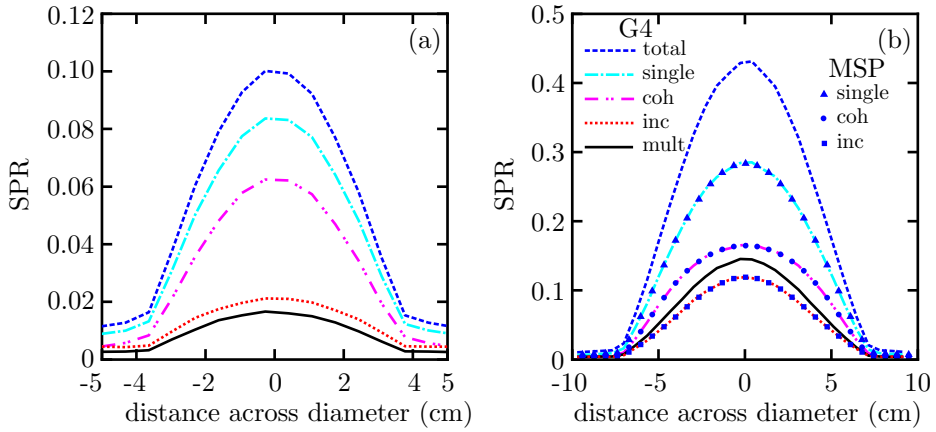

Figure 5.1: Scatter to primary ratios for the central slice across the phantom diameter via the Geant4(G4) simulation for the (a) 7 cm and (b) 14 cm diameter phantoms. In (b) the symbols represent results obtained with the MSP model.

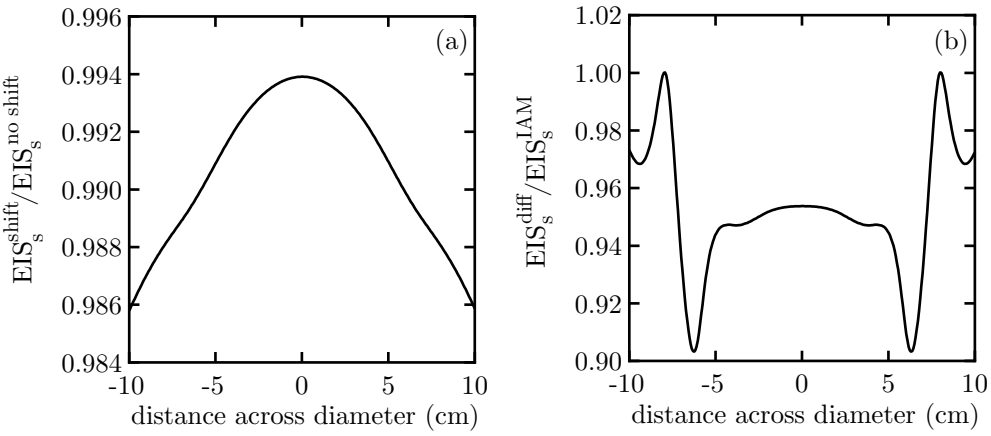

Figure 5.2: Ratios of EIS_s obtained via MSP model calculations for the central slice of the 14 cm diameter phantom: (a) $EIS_s^{\rm inc}$ with Compton shift versus no shift, and (b) $EIS_s^{\rm coh}$ with diffraction versus IAM.

Figure 5.2(a) shows for the 14 cm diameter phantom the ratios of MSP model EIS values due to Compton single scatter with the energy shift (EIS_s^{shift}) versus no shift ($EIS_s^{\text{no shift}}$). The values were close to unity and therefore subsequent model calculations neglected the Compton shift. Figure 5.2(b) shows ratios of model EIS values due to coherent scatter with diffraction effects (EIS_s^{diff}) versus IAM (EIS_s^{IAM}). The use of F extracted from diffraction data reduced the overall energy fluence due to single coherent scattered photons within the projection. The differences in Fig. 5.2(b) suggest that diffraction effects should be incorporated in future simulations.

5.1.2 SSP versus Geant4

The potential use of the SSP model is first presented using non-diffraction data as it was for the Geant4 simulations. Figure 5.3 shows the peak EIS SPR calculated via the model with different values of δ for the (a) 7 cm and (b) 14 cm diameter cylinders. The horizontal dotted lines represent the peak SPRs obtained via Geant4. For approximating the Geant4 peak SPR for the total scatter signal with the 7 cm diameter phantom a $\delta = 0.5585$ is best whereas $\delta = 0.4541$ was found for the SPR due solely to single scatter. For the 14 cm diameter phantom, the corresponding δ's were 0.5455 (total) and 0.4237 (single).

Using these values of δ in the SSP model, Fig. 5.4 shows the SPR for three different detector slices: (a,d) central slice (i.e. #150), (b,e) #100 and (c,f) #85 (near the phantom end). The top and bottom panels are respectively for the 7 cm and 14 cm diameter phantoms. The values of δ obtained by matching the peak SPR reproduced the Geant4 SPRs of these three slices satisfactorily. However, the SPRs calculated via the SSP model for the off center slices were underestimated slightly more for the 14 cm diameter cylinder. A subtraction of the model single scatter EIS values from the model total scatter EIS values provided an estimate of the multiple

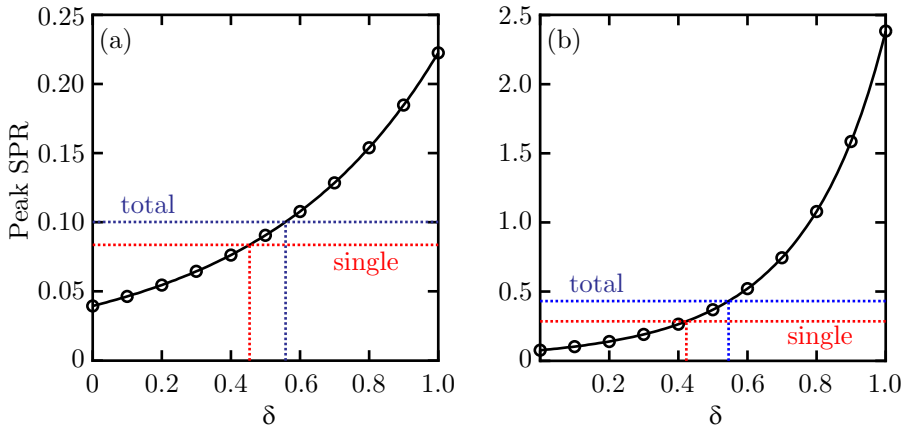

Figure 5.3: Peak scatter to primary ratios obtained with the SSP model for different values of δ for the (a) 7 cm and (b) 14 cm diameter phantoms. Dotted lines show the peak SPR values obtained via Geant4 simulations.

scatter component. The multiple scatter SPR via the model approximated the Geant4 one reasonably well.

5.1.3 SSP versus MSP

In this section only model calculations were performed to assess the effects on SPR and δ when the cylinder mass fractions varied from 100%:0% to 0%:100% in steps of 10%. Figures 5.5(a) and (b) show the single scatter central slice SPRs obtained via the MSP model for the 7 cm diameter phantom using respectively IAM and Diff form factors. Figures 5.5(c) and (d) show corresponding results for the 14 cm diameter phantom. As the fat content increases the SPRs for all cases decrease. The ratios of the peak SPRs 100:0 to 0:100 were: 1.38 (7 cm-IAM), 1.33 (14 cm-IAM), 1.19 (7 cm-Diff), and 1.20 (14 cm-Diff).

Figure 5.6 shows the values of δ obtained from SPR peak matching as a function of ν_{fib}. Results are shown for the 7 cm and 14 cm diameter cylinders both via IAM and Diff F. Each combination of diameter and form factor data yielded a different

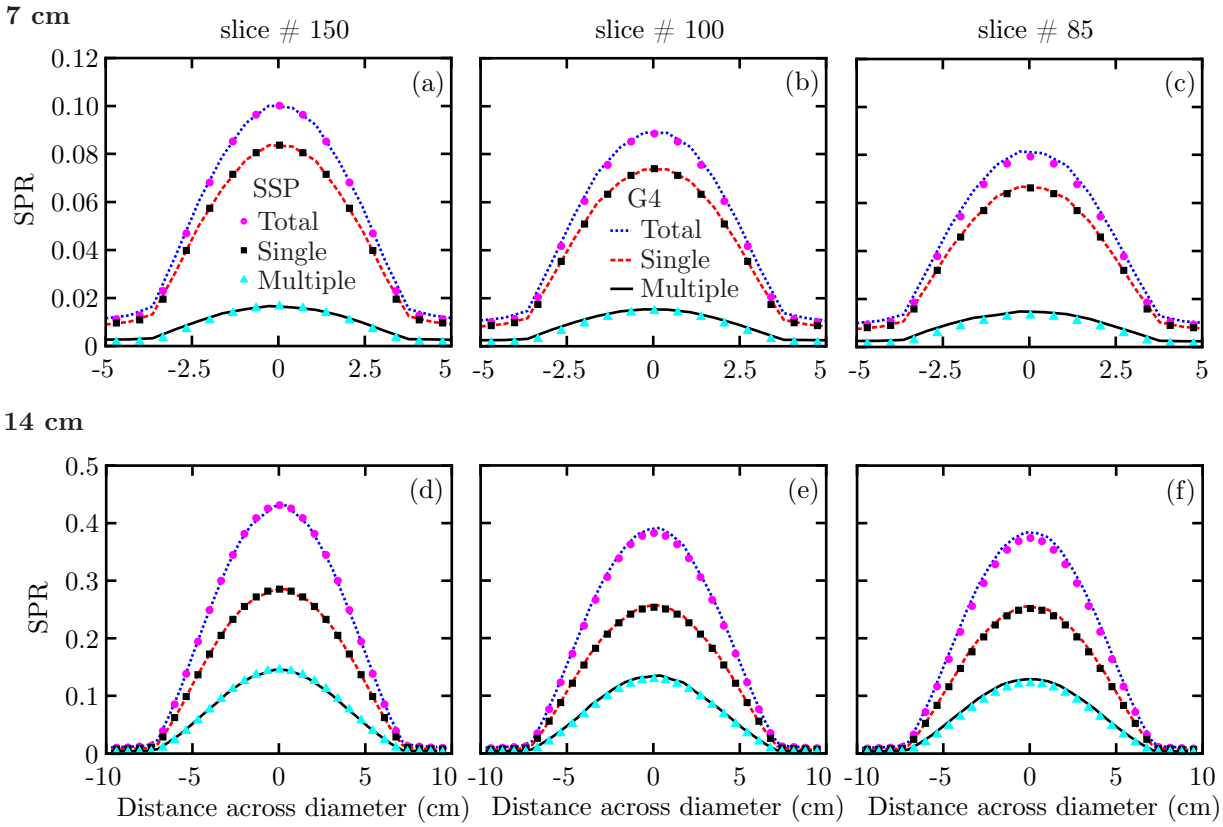

Figure 5.4: Scatter to primary ratios via the SSP model compared to Geant4 for three slices; from the (a,b,c) 7 cm and (d,e,f) 14 cm diameter phantoms. The data points refer to the results produced by the SSP model, while the lines refer those produced by Geant4 simulations.

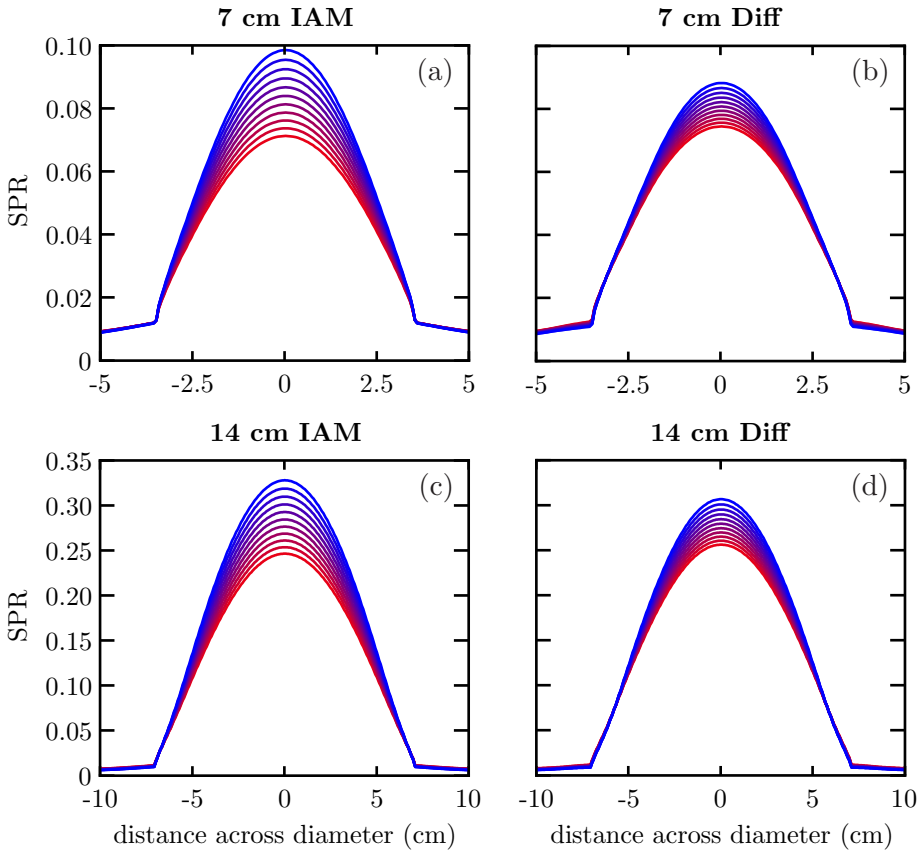

Figure 5.5: Single scatter SPR via MSP model for the 7 cm diameter phantom (a) via IAM and (b) Diff form factors. (c) and (d) corresponding ones for the 14 cm diameter phantom. The curves from top to bottom correspond to cylinders with $\nu_{\text{fib}} = 100\%$ to 0% in steps of 10%.

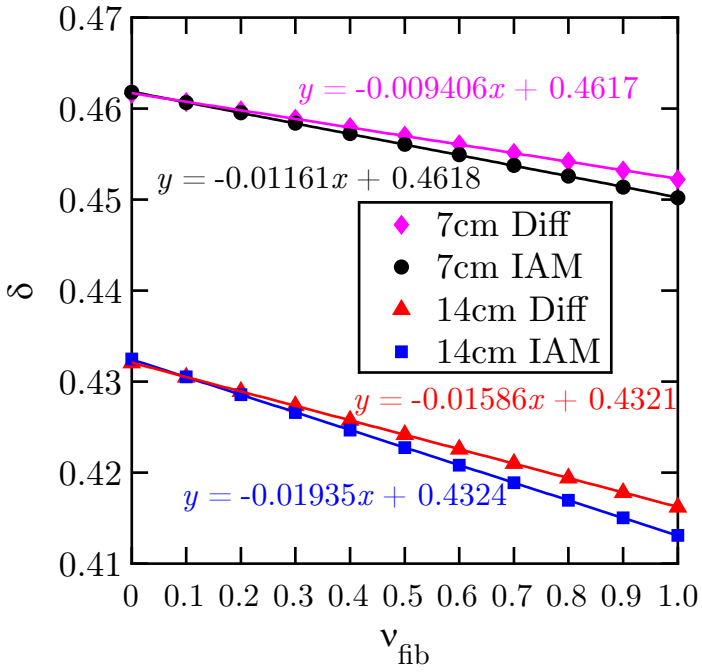

Figure 5.6: δ as a function of ν_{fib} for the 7 cm and 14 cm diameter phantoms using the IAM and Diff form factors.

linear relationship of δ versus ν_{fib} of the cylinder.

Using the δ's for the 80:20 and 20:80 compositions, Fig. 5.7 shows their single scatter SPRs for three different detector slices: (a,d) central slice (i.e. #150), (b,e) #100 and (c,f) #85. The top and bottom panels are respectively for the 7 cm and 14 cm diameter phantoms. The values of δ obtained by matching the peak SPR reproduced the MSP SPRs of these three slices satisfactorily. As seen before, with the off-center slices the SSP tends to underestimate the SPR. This effect is more visible for the thicker phantom.

5.2 Potential Use of the SSP Model

5.2.1 14 cm Diameter Cylinder with 21 Embedded Small Axial Cylinders

The top panels of Fig. 5.8 shows slice #129 cross sectional images of the phantom. The images were generated using four different types of radon transforms: (a) λ_p, (b) λ_t, (c) λ_{t-s} using SSP $\delta_{\text{single}}^{14,50:50} = 0.4237$ and (d) λ_{t-s} using SSP $\delta_{\text{total}}^{14,50:50} = 0.5455$. Evidence of the 5 mm diameter cylinder of fat can be seen at the center of the images. The image via primary [Fig. 5.8(a)] has a more uniform appearance in the 0.5:0.5 region whereas the one which includes primary, single scatter and multiple scatter [Fig. 5.8(b)] has an intensity profile which varied from the center to the edge. The variation was minimized in Fig. 5.8(c) which was obtained via correction for some single scatter via the SSP $\delta_{\text{single}}^{14,50:50} = 0.4237$. The image corrected via SSP $\delta_{\text{total}}^{14,50:50} = 0.5455$ [Fig. 5.8(d)] was similar to the image via primary.

The bottom panels of Fig. 5.8 show corresponding central line profiles through the images. The cupping artifact is evident clearly in Fig. 5.8(b) and to a lesser extent

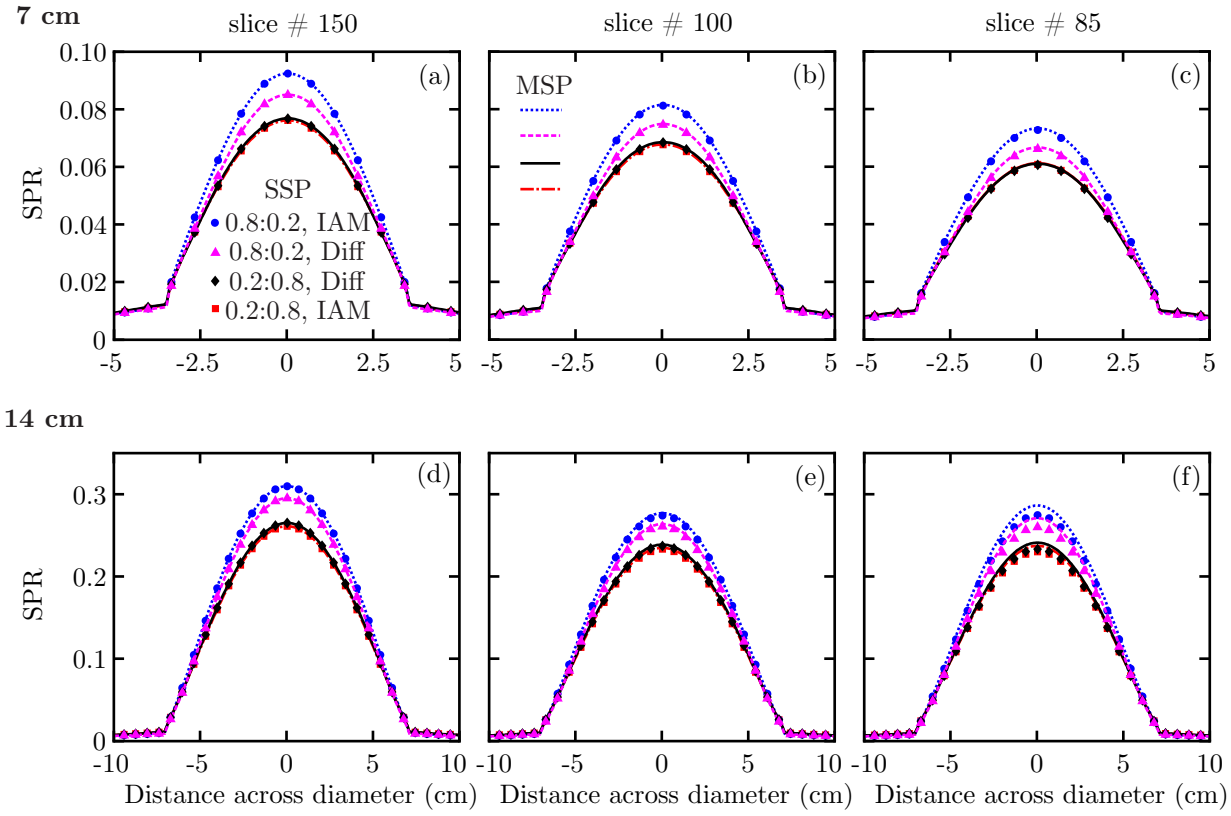

Figure 5.7: Scatter to primary ratios via the SSP and MSP models for three slices; (a,b,c) 7 cm and (d,e,f) 14 cm diameter phantoms. The data points refer to the results produced by the SSP model, while the lines are those produced by the MSP model.

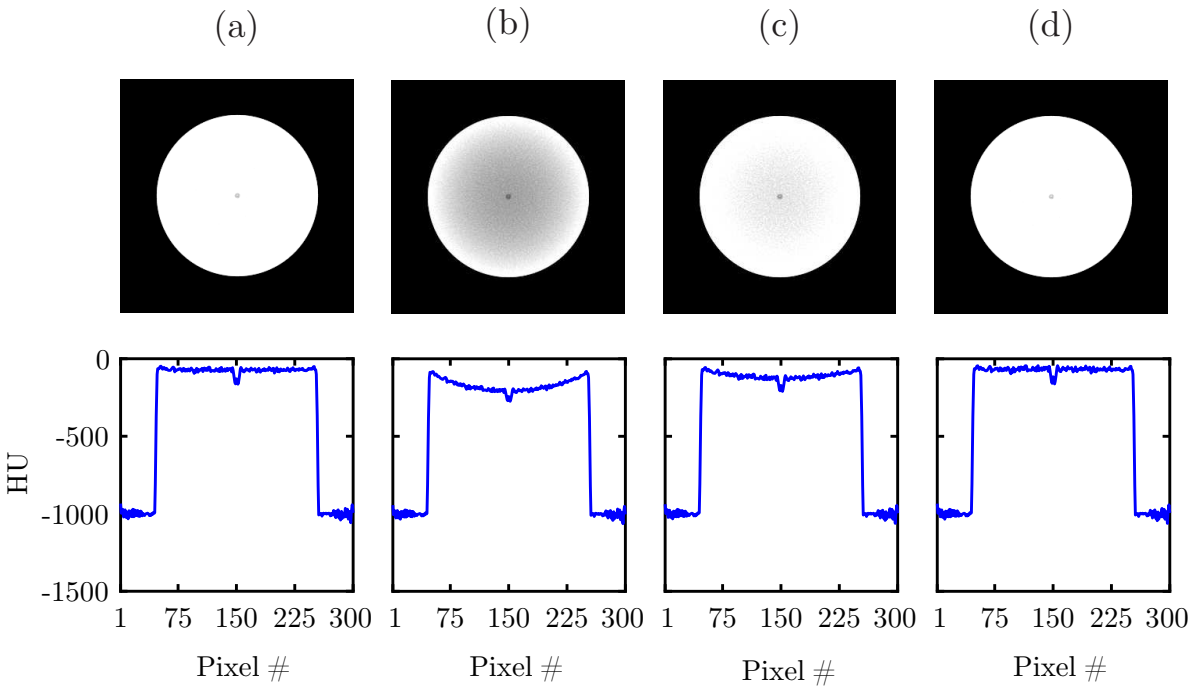

Figure 5.8: Top panels are cross sectional images (slice #129) of the 14 cm diameter phantom with 21 embedded cylinders using four different types of radon transforms: (a) λ_p, (b) λ_t, (c) λ_{t-s} using SSP $\delta_{\text{single}}^{14,50:50} = 0.4237$, and (d) λ_{t-s} using SSP $\delta_{\text{total}}^{14,50:50} = 0.5455$. The bottom panels are corresponding central HU line profiles through the images.

in Fig. 5.8(c). The similarity between Figs. 5.8(a) and (d) with no cupping artifact suggest a potential use of the SSP for minimization of the cupping artifact.

Figure 5.9 shows the CT HUs along the central axis of the cylinder. The HUs corresponding to the two segments at the ends of the cylinder were not shown in the figure because of edge effects. The HUs via primary shown with no noise and with noise are the values which one would try to seek via post scatter correction methods. Clearly the values obtained using no correction method for scatter results in unreliable HUs. The application of the SSP for correction of total scatter yielded a curve which followed that of the primary. The results suggest some potential use of the SSP model and the analysis in the next section with the 14 cm diameter cylinder with 5 embedded cylinders will also support this finding.

5.2.2 14 cm Diameter Cylinder with 5 Large Embedded Cylinders

The use of the SSP model with a homogeneous phantom to correct for single scattered x rays during CBCT of heterogeneous phantoms is now demonstrated. Figure 5.10 shows the ratios of $EIS_s^{\mathrm{MSP}}/EIS_s^{\mathrm{SSP}}$ for the 14 cm phantoms with overall compositions of (a-b) $m_{\mathrm{fib}} = 86.4$ phantom and (c-d) 16.5. The MSP projection is for projection angle 0°. The ratios closest to unity occurred when the SSP model used a δ corresponding to the m_{fib} of the heterogeneous phantom. However, even for the case where the MSP and SSP model were for the same m_{fib} composition there are obvious differences between them. However, these minor differences will be shown to have little effect on the successful application of the SSP model in correcting the cupping artifact upon reconstruction.

Figure 5.11 shows the CT images obtained for two slices via the use of four Radon transforms for both heterogeneous phantom configurations. Qualitatively,

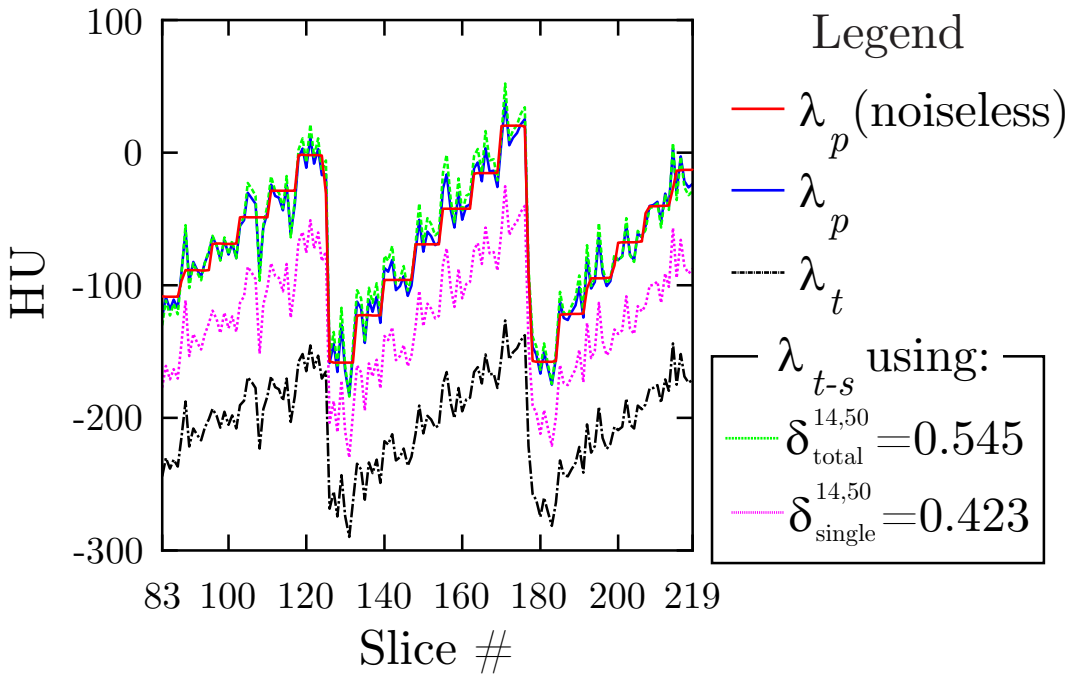

Figure 5.9: HUs along the central axis of the 14 cm diameter phantom with 21 embedded axial cylindrical segments. Due to edge effects, values at the ends of the phantom were omitted.

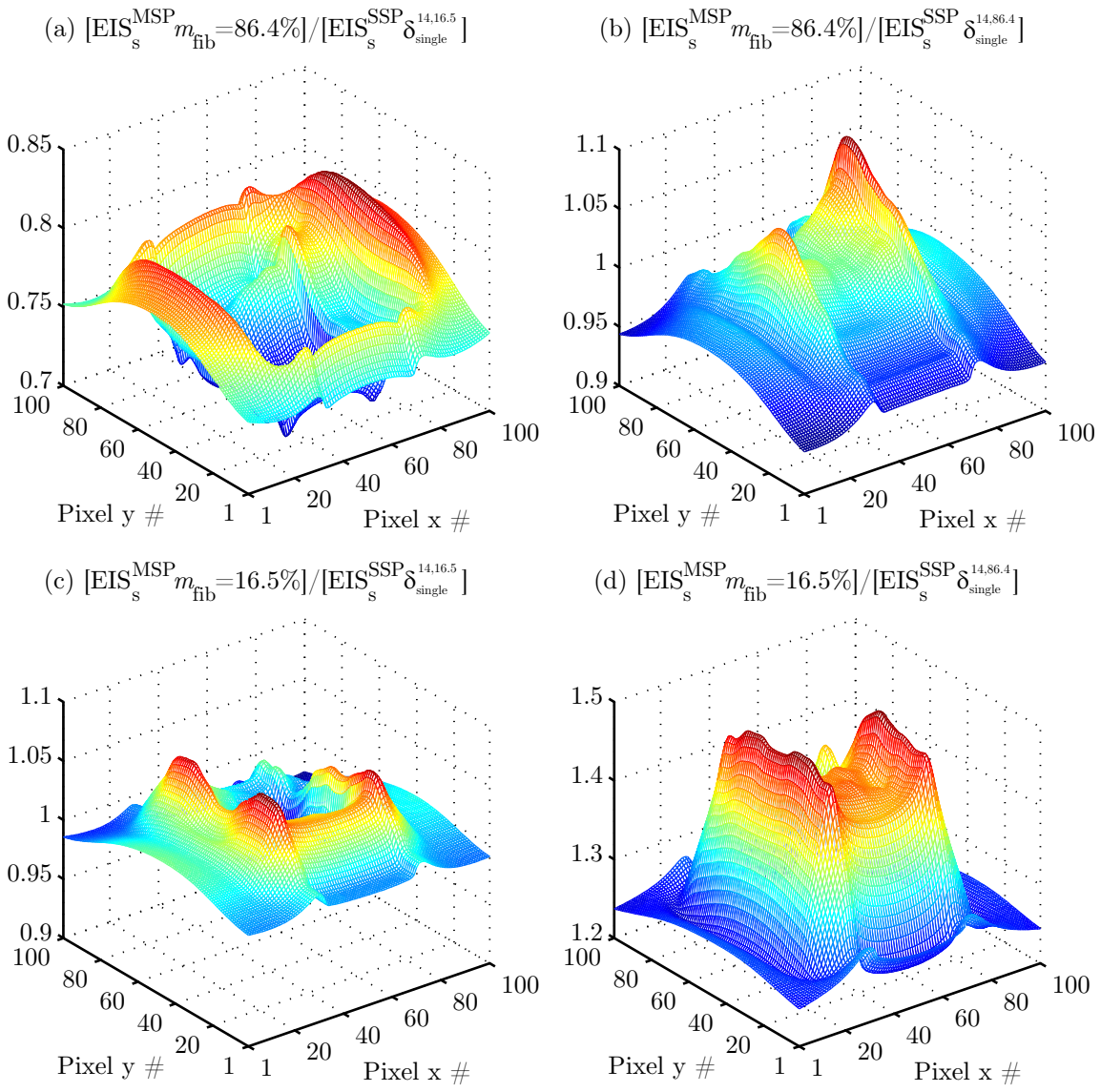

Figure 5.10: Ratios of EIS_s^{MSP}/EIS_s^{SSP} for both configurations of the heterogeneous phantom using two different SSP model calculations.

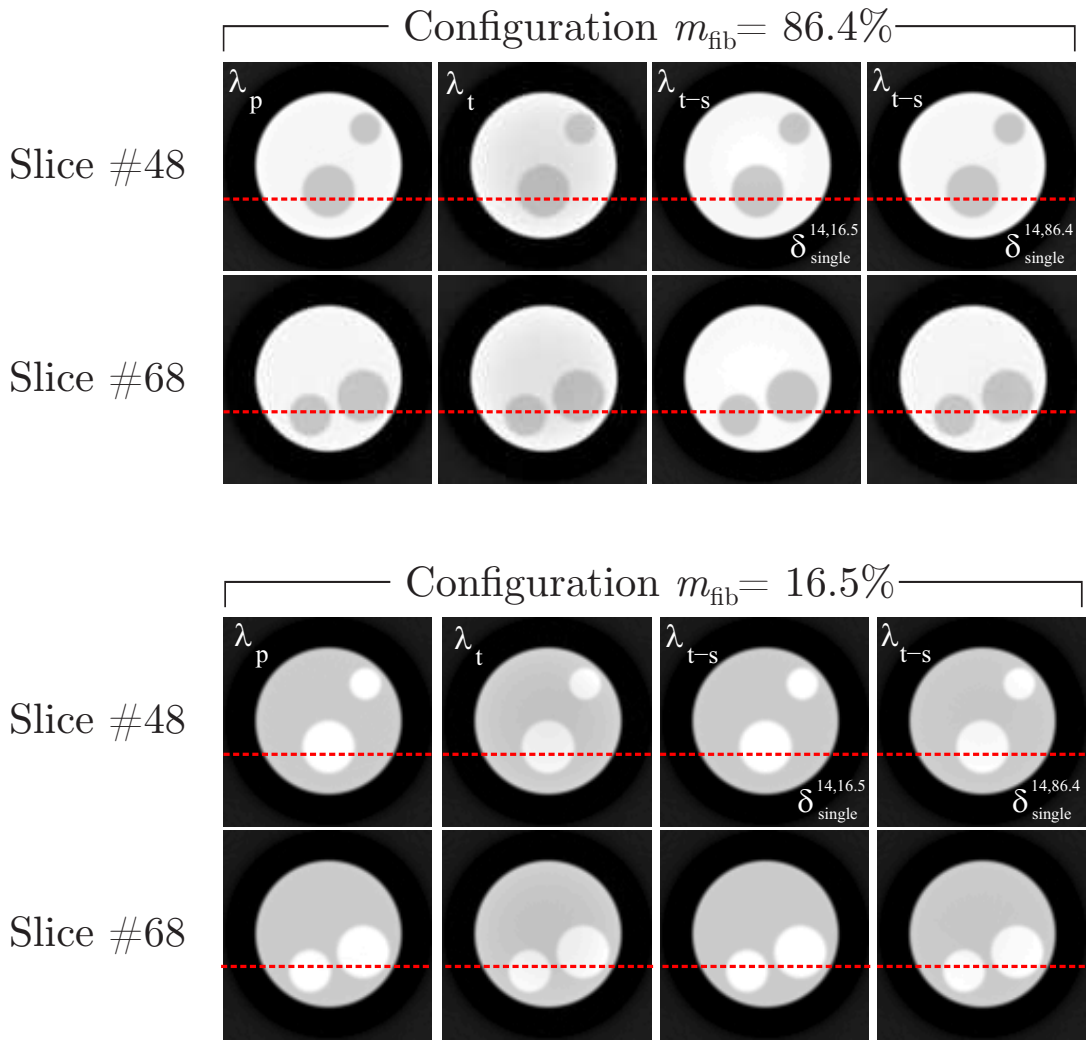

Figure 5.11: Cross sectional images of heterogeneous phantoms using four different types of radon transforms. The top set of eight reconstructed images are for phantom $m_{\text{fib}} = 86.4$ while the bottom images are for $m_{\text{fib}} = 16.5$.

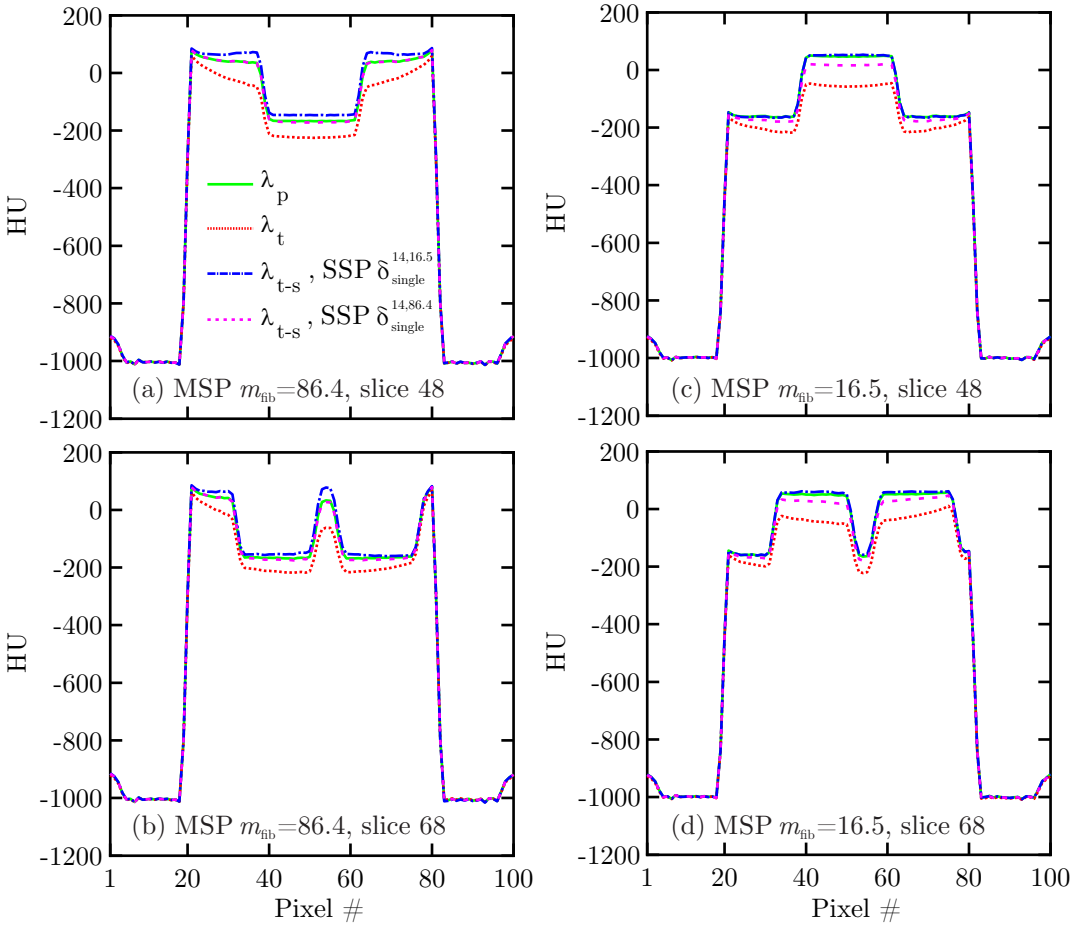

Figure 5.12: Line profiles through images shown in Fig. 5.11: heterogeneous phantoms (a-b) $m_{\text{fib}} = 86.4$ and (c-d) $m_{\text{fib}} = 16.5$.

the images obtained using λ_p and λ_{t-s} with the δ obtained using the m_{fib} of the configurations were more uniform. The dashed lines in the images have been added to indicate the location of the line profiles shown in Fig. 5.12. Clearly the use of λ_t gives a line profile with a pronounced cupping artifact whereas those using λ_{t-s} showed a great reduction of this artifact. Again the λ_{t-s} with the correct δ matched the corresponding primary well, showing the SSP model's ability to correct the cupping artifact.

Table 5.1 summarizes fib and fat Hounsfield units and their associated standard deviations (σ) obtained using four different types of projections for the 5 embedded cylinders in a homogeneous cylinder. Columns 3 and 4 are the values obtained using primary photons and these HUs are what would be sought using scatter correction methods. Larger standard deviations occurred for case of fibrous embedded cylinders in a fat cylinder (with overall $m_{\text{fib}} = 16.5$). Radon transforms not corrected for scatter yielded CT numbers (columns 5 and 6) falling out of range of the desired ones. For the phantom with $m_{\text{fib}} = 86.4$, the CT numbers obtained using a correct $\delta = 0.418$ for the SSP model yielded good results, better than those obtained with $\delta = 0.429$ as could be expected. These results showed that the SSP model can be used to correct for scatter during CBCT of heterogeneous phantoms provided an estimate of m_{fib} is known.

Phantom Composition		λ_p		λ_t		λ_{t-s}			
						$\delta_{\text{single}}^{14,86:14} = 0.4184$		$\delta_{\text{single}}^{14,17:83} = 0.4295$	
m_{fib}	m_{fat}	fib	fat	fib	fat	fib	fat	fib	fat
16.5	83.5	48.5	-159	-46.6	-215	19.9	-178	52.3	-161
		3.18	23.0	18.9	34.0	9.64	26.5	3.67	23.3
86.4	13.6	37.8	-164	-38.2	-214	38.5	-169	77.1	-147
		7.47	2.39	24.6	12.3	7.58	3.61	15.4	7.22

Table 5.1: HU values and standard deviations (σ) obtained using different radon transforms λ. Dual numbers in cell blocks: HU-top, σ-bottom.

Chapter 6

Discussion

The preliminary results obtained with the scattering point models were interesting. The potential use of the SSP model to subtract scatter contributions from raw projections was demonstrated. The Hounsfield Units (HU) post-scatter correction agreed well with those obtained with primary photons. The correction with the SSP model works best when the mass fractions of fib and fat of the heterogeneous phantom are known. The fast computation time of the SSP model (e.g. 373 seconds to generate a single profile) would make it a prime candidate for an iterative algorithm designed to correct for scatter.

Although only single scatter and primary signals were included in the image analysis, the comparison of the Geant4 to SSP model results showed that the SSP model can potentially approximate the total scatter. A future work will consist of obtaining a δ versus m_{fib} relationship by matching the SSP SPRs with total scatter Geant4 SPR data. These δ versus m_{fib} fits will then be used as they were here for heterogeneous phantoms. Since the incorporation of the diffraction effects into the model calculations changed the SPR, Geant4 analysis will need to include diffraction effects.

Although the heterogeneous phantom consisting of cylinders used in this study was simplistic, it served the purpose of demonstrating the potential use of the SSP model. More realistic shaped voxelated phantoms of various diameters will be investigated. Geant4 computations to obtain 300 projections are not generally feasible and that is the purpose of the MSP model which allows the single scatter to be obtained. The CPU time required to generate the 300 single scatter fields for one heterogeneous phantom via the MSP was 20.4 days which is manageable through using SHARCNET's MPI (Message Passing Interface) computing solutions. The Geant4 analysis will be used to validate the MSP model for more realistic phantoms and also estimate the multiple scatter which will most likely not be a function of the projection angle. Two Geant4 runs at different angles can serve the purpose of showing that multiple scatter is not a function of projection angle but mostly of the phantom composition and size when it comes to its effects on the cupping artifact and CT numbers.

The breast CBCT scatter models presented here would require an estimate of the composition of the main phantom. An estimates can be achieved via breast density assessments with CBCT[13] or via a similar method as in Ref. [35]. Future work will consist of implementing corrections for breast density.

Accurate scatter cross section data are needed in order to advance the findings in this work. A custom built CdTe biopsy diffractometer and associated wide-angle x-ray scatter (WAXS) fat subtraction protocol will be used to acquire scatter data for breast tissue.[35, 36] The incident spectrum used in the calculations must be same as that used during image acquisition. Scatter techniques to measure N_0 can be applied.[36, 37]

Chapter 7

Conclusion

The main objective of this research work was to develop simplified scattering point models which could provide an estimate of the scatter field during breast CBCT scans. The multiple scattering point model along with the more simplified single scattering point model were compared to Geant4 results for scenarios using homogeneous breasts, and both were able to provide acceptable estimates of the Geant4 simulated SPRs. The SSP model slightly underestimated the scatter signals further from the central slice. The SSP model was also tested for correcting scatter contamination in scenarios of heterogeneous breasts, where the inner structure was treated as unknown. This scatter correction was successful in reducing the cupping artifact from the reconstructed images so long as the overall composition of the breast was known. The accuracy of the reconstructed HU values improved in these scatter corrected images when compared to an ideal scatter-free reconstruction.

Analysis of CBCT images following corrections for scatter via the SSP model with different δ's could provide an iterative approach to obtain higher quality CBCT images and estimates of the breast density. The tools (i.e. models/Geant4/C++ software/Matlab) devised in this work will be extended for an in-depth computational analysis which will help advance the research towards clinical applications.

The scatter correction techniques presented in this work would require no additional measurements on the patient and therefore no extra dose.

Ultimately, a simplified scattering point model was shown to be able to provide quick and acceptable estimations of the scatter signal. The findings with the scatter models presented in this work were promising and further investigations are warranted.

Appendix A

MSP Model Code Segment

The following C++ code sample encompasses the core of the MSP model calculations. Outside of the provided code, other key aspects of the program are a simple message passing interface (mpi) for parallel computations as well as various helper functions. Some examples of the helper functions employed are basic μ and μ_s calculations, vector/ray operations, and ray-shape intersection calculations. These elementary helper functions are not included in the following sample for the sake of brevity.

```
//Scatter along beamlets defined by each of these detector pixels
for(vector<detectorPixel*>::iterator pxl=detector.begin();
     pxl!=detector.end(); pxl++){

 //These vectors contain information on which phantom volumes this
 // source-pixel beamlet passes through (filled elsewhere).
 // These three vectors are of the same length, and indices
 // can be used equivalently between them
 vector<int> physVolOrder;//index values for physVol array
 // Order of physical volumes the source-pixel ray passes through
```

```
// Includes the phantom, as well as sub-structure
// Contains separate values for volumes intersected multiple times
vector<double> intersectsSorted;//in range [0,1]
// Fractional distance along ray
vector<double> intersectLengthsSorted;//in cm
// Distance from source along ray

//subdivide each physical volume the ray passes
// through into scattering points
for(int pv=0; pv<physVolOrder.size(); pv++){

 Vector3D sourceToScatterBegin = intersectsSorted[pv] * (*pxl)->sourceToPixel;
 Vector3D sourceToScatterEnd = intersectsSorted[pv+1] * (*pxl)->sourceToPixel;

 double totalIntersectLength =
      (intersectLengthsSorted[pv+1]-intersectLengthsSorted[pv]);
 //At least 1 scattering point per 1cm of intersection with material
 int numScatteringPoints = ceil(totalIntersectLength / 1.f);
 double totalIntersectionLength_delta = totalIntersectLength /
      (double)numScatteringPoints;

 Vector3D scatterStartToEnd_delta =
      (sourceToScatterEnd - sourceToScatterBegin) *
          (1.f / numScatteringPoints);

 for(int n=0; n<numScatteringPoints; n++){
  Vector3D sourceToScatter = sourceToScatterBegin +
```

```
    scatterStartToEnd_delta * n +
            scatterStartToEnd_delta * 0.5;

//Scatter from current scattering point to every pixel
for(vector<detectorPixel*>::iterator pxl2=detector.begin();
    pxl2!=detector.end(); pxl2++){

 //Don't scatter to the same pixel as the beamlet
 if(pxl == pxl2) continue;

 Vector3D scatter2pixelVec = (*pxl2)->sourceToPixel - sourceToScatter;

 //Calculate the solid angle of the detector pixel from scattering point
    // using the dot product to find cos(alpha)
 double dotProduct = ( detectorNormal*(-1*scatter2pixelVec) ) /
         ( detectorNormal.Length() * scatter2pixelVec.Length() );
 double solidAngle = (*pxl2)->area_cm2 * dotProduct /
         scatter2pixelVec.LengthSqd();

 //Calculate the length of phantom material the beam needs
    // to traverse to reach the pixel
 double secondaryIntersects[2];
 Ray3D scatter2pixelRay(sourcePos+sourceToScatter,//ray start
     sourcePos+sourceToScatter + scatter2pixelVec);//ray end
 Intercepts(phantomVol, scatter2pixelRay, secondaryIntersects);
 double exitLength = (secondaryIntersects[1]-secondaryIntersects[0]) *
     scatter2pixelRay.Length();
```

```
double cos_scattering_angle = (sourceToScatter*scatter2pixelVec) /
     (sourceToScatter.Length()*scatter2pixelVec.Length());
double angle_deg = acos(cos_scattering_angle)*180.f/pi;

//For each energy in the spectrum
for(int ihv=0; ihv<hvset.size(); ihv++){
 double MuDPartial = 0;
 //Include attenuation from all volumes up to the 'current' one,
 // as well as the partial passage through current volume
 for(int pv2=0; pv2<=pv; pv2++){
  if(pv2==pv){
   MuDPartial += physVol[physVolOrder[pv2]]->mu[ihv] *
         (intersectLengthsSorted[pv2+1]-intersectLengthsSorted[pv2]) *
         n/(double)numScatteringPoints;
  } else {
   MuDPartial += physVol[physVolOrder[pv2]]->mu[ihv] *
         (intersectLengthsSorted[pv2+1]-intersectLengthsSorted[pv2]);
  }
 }

 double mu = physVol[physVolOrder[pv]]->mu[ihv];

 //Basic scatter calculation
 // using average mu value of phantom to attenuate beam
 (*pxl2)->Ns[ihv] += (*pxl)->frac_N0 * phi0[ihv] * exp(-MuDPartial) *
    ( 1 - exp( - mu * totalIntersectionLength_delta ) ) *
```

```
        physVol[physVolOrder[pv]]->muS(angle_deg,ihv) * solidAngle / mu *
        exp(-muAvg[ihv] * exitLength);

    }
   }
  }
 }
}
```

Appendix B

On the Concept of KERMA and Absorbed Dose

One of the most important concepts in any medical application of ionizing radiation is that of its effects upon the patient. When x rays interact with matter, as described in Chapter 2, energy is transferred to the patient tissue medium. This process of energy transfer can be generally viewed as a two stage process. First, an incident photon interacts with an atom and transfers energy into freeing an electron or electrons with an amount of kinetic energy. Then in the second stage, these energetic freed electrons deposit their energy back into the medium through excitation and ionization. [38]

This first stage, consisting of setting the electron(s) into motion, is quantized as the Kinetic Energy Released in the Medium (KERMA, or simply K). This value is defined as

$$K = \frac{\mathrm{d}\overline{E_{\mathrm{tr}}}}{\mathrm{d}m} \tag{B.1}$$

where $\mathrm{d}\overline{E_{\mathrm{tr}}}$ is the kinetic energy transferred to the freed electrons in the volume element of mass $\mathrm{d}m$. This quantity has dimensions of energy/mass, and as such the SI units are joules per kilogram (J/kg). For a monoenergetic beam of photons with

fluence Φ, the kerma generated can be calculated by

$$K = \Phi \left(\frac{\mu}{\rho} \right) \overline{E_{\text{tr}}} \tag{B.2}$$

where $\frac{\mu}{\rho}$ is the mass attenuation coefficient of the medium for this photon energy, and $\overline{E_{\text{tr}}}$ is the average energy transferred to the electrons when these photons undergo interaction. Since this is an energy-specific calculation, and x-ray beams are generally polyenergetic, the kerma for an x-ray beam must be calculated via a summation or integration over the photon energies.

The second stage of this energy transfer is quantized as absorbed Dose (D), and is more directly related to the effect on the patient. This quantity is defined as

$$D = \frac{\mathrm{d}\overline{E_{\text{ab}}}}{\mathrm{d}m} \tag{B.3}$$

where $\mathrm{d}\overline{E_{\text{ab}}}$ is the energy absorbed by a mass $\mathrm{d}m$ of the medium. As before, this quantity has dimensions of energy/mass, but has a special unit called the Gray (Gy), where 1 Gy is equal to 1 J/kg. The dose is not directly equivalent to the kerma since an energetic freed electron travels a non-negligible distance as it deposits its energy through the excitation and ionization of atoms along its path. It's also important to note that not all the energy of this electron is retained in the medium as some is lost through bremsstrahlung radiation. Because of these two factors, while the kerma is straightforwardly calculated through Eq B.2, the absorbed dose cannot be calculated in such a simple manner. The kerma and dose would only be equal in a scenario where the same number of electrons with the same energy distribution are entering and leaving a volume element, along with the energy loss to bremsstrahlung being negligible. Such a scenario is termed as being in electronic equilibrium and is generally not representative of reality, mainly due to the attenuation an x-ray beam undergoes as it travels through a medium. In order to study the absorbed dose in a more realistic scenario it is common to either preform x-ray measurements using a specialized phantom device [39] or Monte Carlo simulations [40].

References

[1] Canadian Cancer Society. Cancer statistics at a glance. `www.cancer.ca/en/cancer-information/cancer-101/cancer-statistics-at-a-glance`, 2015.

[2] J. M. Boone, T. R. Nelson, K .K. Lindfors, and J.A. Seibert. Dedicated breast CT: Radiation dose and image quality evaluation. *Radiology*, 221:657–667, 2001.

[3] W. C. Scarfe and A. G. Farman. What is cone-beam CT and how does it work? *Dent. Clin. North Am.*, 52:707–730, 2008.

[4] L.A. Feldkamp, L.C. Davis, and J.W. Kress. Practical cone-beam algorithm. *J. Opt. Soc. Am. A*, 1(1):612–619, 1984.

[5] J. H. Siewerdsen and D. A. Jaffray. Cone-beam computed tomography with a flat panel imager: Magnitude and effects of x-ray scatter. *Med. Phys.*, 28:220–231, 2001.

[6] A. O'Connell, D. L. Conover, Y. Zhang, P. Seifert, W. Logan-Young, C. L. Lin, L. Sahler, and R. Ning. Cone-Beam CT for Breast Imaging: Radiation Dose, Breast Coverage, and Image Quality. *AJR*, 195:496–509, 2010.

[7] L. Chen, Y. Shen, C. Lai, T. Han, Y. Zhong, S. Ge, X. Liu, T. Wang W. T. Yang, G. J. Whitman, and C. C. Shaw. Dual resolution cone beam breast CT: A feasibility study. *Med. Phys.*, 36:4007–4014, 2009.

[8] S. J. Glick. Breast CT. *Annu. Rev. Biomed. Eng.*, 9:501–526, 2007.

[9] B. Chen and R. Ning. Cone-beam volume CT breast imaging: feasibility study. *Med. Phys.*, 29:755–770, 2002.

[10] A. Karellas and S. Vedantham. Breast cancer imaging: A perspective for the next decade. *Med. Phys.*, 35:4878–4897, 2008.

[11] N. F. Boyd, H. Guo, L. J. Martin, L. Sun, J. Stone, E. Fishell, R. A. Jong, G. Hislop, A. Chiarelli, S. Minkin, and M. J. Yaffe. Mammographic density and the risk and detection of breast cancer. *N. Engl. J. Med.*, 356:227–236, 2007.

[12] C. M. Shafer, E. Samei, and J. Y. Lo. The quantitative potential for breast tomosynthesis imaging. *Med. Phys.*, 37:1004–1016, 2010.

[13] T. Han, C-J. Lai, L. Chen, X. Liu, Y. Shen, Y. Zhong, S. Ge, Y. Yi, T. Wang, W. T. Yang, and C. C. Shaw. Breast density measurement: 3D cone beam computed tomography (CBCT) images versus 2D digital mammograms. In *Proc. of SPIE Vol. 7258: Medical Imaging 2009: Physics of Medical Imaging*, page 72580L(8pp.), 2009.

[14] C. Lai, C. C. Shaw, L. Chen, M. C. Altunbas, X. Liu, T. Jan, T. Wang, W. T. Yang, G. J. Whitman, and S. Tu. Visibility of microcalcification in cone beam breast CT: Effects of x-ray tube voltage and radiation dose. *Med. Phys.*, 34:2995–3004, 2007.

[15] X. Gong, A. A. Vedula, and S. J. Glick. Microcalcification detection using cone-beam CT mammography with a flat panel imager. *Phys. Med. Biol.*, 49:2183–2195, 2004.

[16] X. Gong, S. J. Glick, B. Liu, A. A. Vedula, and S. Thacker. A computer simulation study comparing lesion detection accuracy with digital mammography,

breast tomosynthesis, and cone-beam CT breast imaging. *Med. Phys.*, 33:1041–1052, 2006.

[17] Y. Chen, B. Liu, J.M. O'Connor, C.S. Didier, and S.J. Glick. Characterization of scatter in cone-beam CT breast imaging: Comparison of experimental measurements and Monte Carlo simulation. *Med. Phys.*, 36:857–869, 2009.

[18] K. Kontson and R. J. Jennings. Characterization of scatter magnitude and distribution in dedicated breast computed tomography with bowtie filters. *J. Med Imag.*, 1:033505(13pp.), 2014.

[19] I. Sechopoulos. X-ray scatter correction method for dedicated breast computed tomography. *Med. Phys.*, 39:2896–2903, 2012.

[20] W. Cai, R. Ning, and D. Conover. Scatter correction for clinical cone beam CT breast imaging based on breast phantom studies. *J. X-Ray Sci. Technol.*, 19:91–109, 2011.

[21] M. C. Altunbas, C. C. Shaw, L. Chen, C. Lai, X. Liu, T. Han, and T. Wang. A post-reconstruction method to correct cupping artifacts in cone beam breast computed tomography. *Med. Phys.*, 34:3109–3118, 2007.

[22] P.C. Johns and M.J. Yaffe. X-ray characterization of normal and neoplastic breast tissues. *Phys. Med. Biol.*, 32:675–695, 1987.

[23] R.J. LeClair, Y. Wang, P. Zhao, M. Boileau, and F. Fleurot. An analytic model for the response of a CZT detector in diagnostic energy dispersive x-ray spectroscopy. *Med. Phys.*, 33:1008–1020, 2006.

[24] G. Kidane, R. D. Speller, G. J. Royle, and A. M. Hanby. X ray scatter signatures for normal and neoplastic breast tissues. *Phys. Med. Biol.*, 44:1791–1802, 1999.

[25] M. E. Poletti, O. D. Gonçalves, and I. Mazzaro. X ray scattering from human breast tissues and breast equivalent materials. *Phys. Med. Biol.*, 47:47–63, 2002.

[26] J.H. Hubbell, Wm.J. Veigele, E.A. Briggs, R.T. Brown, D.T. Cromer, and R.J. Howerton. Atomic form factors, incoherent scattering functions, and photon scattering cross sections. *J. Phys. Chem. Ref. Data*, 4:471–538 (1975); Erratum **6** 615–616, 1977.

[27] G. R. Hammerstein, D. W. Miller, D. R. White, M. E. Masterson, H. Q. Woodard, and J.S. Laughlin. Absorbed radiation dose in mammography. *Radiology*, 130:485–491, 1979.

[28] A. H. Narten. X-ray diffraction data on liquid water in the temperature range 4°C-200°C. *Oak Ridge National Laboratory Report No. ORNL*, 4578, 1970.

[29] K. Geraki, M.J. Farquharson, and D.A Bradley. American college of radiology: Breast imaging reporting and data system (birads). *Reston, VA: American College of Radiology*, 1993.

[30] R. Birch, M. Marshall, and G. M. Ardran. Catalogue of spectral data for diagnostic x-rays. *The Hospital Physicists' Association Scientific Report*, Series 30, 1979.

[31] CERN. Livermore low-energy electromagnetic models. `twiki.cern.ch/twiki/bin/view/Geant4/LoweMigratedLivermore`, 2016.

[32] SHARCNET. Shared Hierarchical Academic Research Computing Network. `www.sharcnet.ca`, 2016.

[33] E. F. Plechaty, D. E. Cullen, and R. J. Howerton. Tables and graphs of photon interaction cross sections from 1.0 keV to 100 MeV derived from the LLL eval-

uated nuclear data library, UCRL-50400. Technical report, Lawrence Livermore Laboratory, 1975.

[34] R. Willemink. Multithreaded mex fdk conebeam ct reconstruction algorithm. www.mathworks.com/matlabcentral/fileexchange/23314-multithreaded-mex-fdk-conebeam-ct-reconstruction-algorithm, 2009.

[35] R. Y. Tang, N. McDonald, C. Laamanen, and R. J. LeClair. A method to estimate the fractional fat volume within an ROI of a breast biopsy for WAXS applications: Animal tissue evaluation. *Med. Phys.*, 41:113501(8pp.), 2014.

[36] R. Y. Tang, C. Laamanen, N. McDonald, and R. J. LeClair. WAXS fat subtraction model to estimate differential linear scattering coefficients of fatless breast tissue: Phantom materials evaluation. *Med. Phys.*, 41:053501(7pp.), 2014.

[37] K. Maeda, M. Matsumoto, and A. Taniguchi. Compton-scattering measurement of diagnostic x-ray spectrum using high-resolution Schottky CdTe detector. *Med. Phys.*, 32:1542–1547, 2005.

[38] H. E. Johns and J. R. Cunningham. *The Physics of Radiology.* Charles C. Thomas, Publisher Ltd, 4th edition, 1983.

[39] J. Begg V. Nelson P. Metcalfe A. Quinn, L. Holloway. Kilovoltage cone-beam CT imaging dose during breast radiotherapy: a dose comparison between a left and right breast setup. *Med. Dosim.*, 39:190–193, 2014.

[40] J. M. Boone, N. Shah, and T. R. Nelson. A comprehensive analysis of DgN_{ct} coefficients for pendant-geometry cone-beam breast computed tomography. *Med. Phys.*, 31:226–235, 2004.